A new proposal to the Jefferson Lab Program Advisory Committee (PAC33)

Precision Measurement of the Neutron Magnetic Form Factor up to $Q^2 = 8.0$ (GeV/c)^2 by the Ratio Method

G.B. Franklin, B. Quinn (spokesperson),
R. Schumacher, S. Riordan, B. Vernarsky
Carnegie Mellon University, Pittsburgh, PA 15213

A. Camsonne, J.P. Chen, E. Chudakov, C. DeJager,
P. Degtyarenko, J. Gomez, O. Hansen, D. W. Higinbotham,
J. LeRose, R. Michaels, S. Nanda, A. Saha, V. Sulkosky,
B. Wojtsekhowski (spokesperson and contact person)
Thomas Jefferson National Accelerator Facility, Newport News, VA 23606

C.F. Perdrisat, L.P. Pentchev
College of William and Mary

E. Cisbani, F. Cusanno, F. Garibaldi,
S. Frullani, G. M. Urciuoli, M. Iodice, M.L. Magliozzi
INFN, Rome, Italy

D. Day, R. Lindgren, N. Liyanage,
V. Mamyan, B. E. Norum, K. D. Paschke
University of Virginia, Charlottesville, VA 22901

W. Brooks
Universidad Tecnica Federico Santa Maria, Valparaiso, Chile

V. Punjabi, M. Khandaker, F. Wesselmann
Norfolk State University

W. Boeglin, P. Markowitz, J. Reinhold
Florida International University, Fl

J. Annand, D. Hamilton, D. Ireland, R. Kaiser, K. Livingston,
I. MacGregor, B. Seitz, and G. Rosner
University of Glasgow, Glasgow, Scotland

D. Nikolenko, I. Rachek, Yu. Shestakov
Budker Institute, Novosibirsk, Russia

R. De Leo, L. La Gamba, S. Marrone, E. Nappi
INFN, Bari, Italy

M. Mihovilovič, M. Potokar, S. Širca
Jožef Stefan Institute and Dept. of Physics, University of Ljubljana, Slovenia

J. Lachniet
Old Dominion University, Norfolk, VA

J. Gilfoyle
University of Richmond, Richmond, VA

E. Piasetzky, G. Ron
Tel Aviv University, Israel

A. Glamazdin
Kharkov Institute of Physics and Technology, Kharkov 310077, Ukraine

J. Calarco
University of New Hampshire, Durham, NH 03824

B. Vlahovic
North Carolina Central University, Durham, NC 03824

A. Sarty
Saint Mary's University, Nova Scotia, Canada B3H 3C3

K. Aniol and D. J. Magaziotis
Cal State University, Los Angeles, CA 90032

S. Abrahamyan, A. Ketikyan, S. Mayilyan, A. Shahinyan, H. Voskanyan
Yerevan Physics Institute, Yerevan, Armenia

and **The Hall A Collaboration**

December 10, 2007

Abstract

We propose to make a high-precision measurement of the neutron's magnetic form factor, G_M^n , at six kinematic points: $Q^2 = 3.5,\ 4.5,\ 5.25,\ 6.0,\ 7.0$ and 8.0 $(\text{GeV/c})^2$. Little data on G_M^n exists in this kinematic range and the existing data have large systematic uncertainties. In the proposed experiment, systematic errors are greatly reduced by the use of the "ratio" method in which G_M^n is extracted from the ratio of neutron-coincident to proton-coincident quasi-elastic electron scattering from the deuteron. The experiment would be performed in Hall A using the BigBite spectrometer to detect the scattered electrons and the BigHAND to detect both neutrons and protons. A large aperture dipole magnet on the nucleon flight path will greatly enhance particle identification by slightly deflecting the protons. Calibration reactions will be used to produce tagged neutrons and protons at essentially the same momentum as the quasi-elastic nucleons. The efficiency of BigHAND is expected to be high and stable and to be well calibrated. Projected systematic errors are below 3% on the measured ratio of cross sections (1.5% on the extracted form factor) and we aim for statistical errors at a similar level. We request a total of 28 days divided among three beam energies.

Contents

1 Introduction

The elastic form factors of the nucleons give us some of the best opportunities to make precise measurements related to the structure of hadrons. In the one-photon approximation the cross section for scattering of electrons from a spin-$\frac{1}{2}$ target can be written as

$$\frac{d\sigma}{d\Omega} = \eta \frac{\sigma_{\text{Mott}}}{1 + \tau} \left((G_E)^2 + \frac{\tau}{\epsilon}(G_M)^2 \right)$$

where
$\eta = \frac{1}{1 + 2\frac{E}{M_N}\sin^2(\theta/2)}$ is the recoil factor
$\epsilon = (1 + \vec{q}^2/Q^2 \tan^2(\theta/2))^{-1} = (1 + 2(1 + \tau)\tan^2(\theta/2))^{-1}$ is the longitudinal polarization of the virtual photon
$\tau = Q^2/4M_N^2$
and $G_E(Q^2)$ and $G_M(Q^2)$ are the Sachs Electric and Magnetic form factors. The measurement of these form factors for the proton and neutron probes their electromagnetic structures.

Little is known of the neutron's magnetic form factor, G_{M}^{n}, (and less of its electric form factor) for $Q^2 > 4$ (GeV/c)^2. We propose to make several high precision measurements of G_{M}^{n} in the range $3.5 < Q^2 < 8.0$ (GeV/c)^2.

Since the form factors are functions only of Q^2, they may be separated by the Rosenbluth technique, making measurements at the same Q^2 but different ϵ to obtain different linear combinations. The apparent failure of this technique in extraction of G_E^p at $Q^2 > 1$ (GeV/c)^2 (as revealed by the recoil polarization method [2,3]) may indicate a failure of the one-photon exchange approximation [4]. This does not invalidate the form given above, however. It just underscores the fact that the corrections may be non-negligible and may become important when trying to separate a small contribution from a larger one. This consideration does not present a great problem when trying to extract the magnetic form factor of the neutron since the electric form factor is generally much smaller.

These Sachs form factors are trivially related to the Dirac and Pauli form factors which are, respectively, the coefficients of the helicity-conserving and -nonconserving currents to which the photon can couple. Non-relativistically the Sachs form factors can be interpreted as the Fourier transforms of the charge and current distributions to which the photon couples in the target. No such simple interpretation is available at higher Q^2. The electric form factor at any Q^2 can still be related to the Fourier transform in the Breit frame. But since the Breit frame is a different frame for each Q^2, this relationship cannot be inverted to extract a charge distribution without a prescription for boosting the nucleon. Recent work [5] by Miller offers an interpretation of the infinite-momentum frame charge density of the nucleon as a function of impact parameter in terms of the Dirac form factor, $F_1 = (G_e + \tau G_m)/(1 + \tau)$. Interestingly, this implies that knowledge of the *magnetic* form factor of the neutron is important to understanding of its charge distribution.

In the approximation that the strange quark does not contribute to the electromagnetic structure of the nucleon, the form factors can be combined [6–8] to extract information about the contributions of individual quark flavors to the electromagnetic structure of the nucleon. Assuming isospin symmetry, the up-quark distribution of the proton is identical to the down-quark distribution of the neutron and *vice versa*. Since the electromagnetic couplings to the individual quarks are known (and the coupling to gluons vanishes) the electric or magnetic form factor of each nucleon can be

written as a linear combination of the electric and magnetic form factors of the two quark flavors. Combining measurements on the neutron and proton then allows direct extraction of the "up" form factor (including contributions from u and $\bar{u}$ quarks from the sea, as well as valence quarks) and the "down" form factor (also composed of all d and $\bar{d}$ contributions). In particular, improved measurements of the neutron's magnetic form factor can be combined with existing measurements of the proton's magnetic form factor to allow extraction of the "up-magnetic form factor" and "down-magnetic form factor". If, on the other hand, the contribution of strange quarks is *not* negligible, then the measurement of the neutron form factors would be critical to allowing the strange contribution to be measured. (At present, however, there are no plans to measure strange form factors in the Q^2 range in which we propose to measure.)

The form factors are pivotal as the meeting place between theory and experiment. Calculations of nucleon structure (as opposed to parameterizations of form factors) can be tested by their ability to predict the experimentally accessible information on nucleon structure reflected in the form factors. (Of course, polarization observables and structure functions will also be relevant.) In particular, lattice QCD predictions will eventually have the capability to make meaningful predictions of hadronic structure. Form factors of the proton and neutron will present important tests of those predictions.

A great deal of experimental and theoretical effort [9–11] is being expended on an ambitious effort to greatly expand the knowledge of nucleon structure by determining the generalized parton distributions. Measurement of form factors plays an important role in that effort since the form factors set the values of sum rules which the generalized parton distributions must obey.

The neutron's form factors are more difficult to measure, of course, because there is no free-neutron target. Spin-asymmetry techniques have been used in extracting the tiny electric form factor of the neutron [12–18] and also in measuring the magnetic [19–21] form factor, particularly at low Q^2. Generally at high Q^2, however, quasielastic scattering from the deuteron has been used [22–37] to extract G_M^n . This is based on the fact that the deuteron is a loosely coupled system, so high-Q^2 quasi-elastic scattering can be viewed as the sum of scattering from a proton target and scattering from a neutron target. This simple picture is complicated only slightly by the fact that the targets are not at rest but are moving with the "Fermi motion" intrinsic to the deuteron's wave-function.

Several techniques have been used to try to isolate the electron-neutron scattering of interest. In the "proton-subtraction" technique [22–27] single-arm quasi-elastic electron scattering from the deuteron is measured. This is combined with a measurement of single-arm elastic scattering from the proton. An attempt is made to fold in the expected effects of Fermi motion to simulate the expected contribution of the proton in the measured quasi-elastic spectrum. This is then subtracted and the remainder is interpreted as a measure of quasi-elastic electron scattering off the neutron from which the (almost purely magnetic) form factor can be determined. This technique tends to suffer from the error-propagation problems intrinsic to subtraction of two large numbers. At low Q^2 the proton electric form factor dominates (and the proton magnetic form factor is never small compared to the neutron's). At high Q^2 inelastic background becomes a serious problem, to the extent that the quasi-elastic "peak" may not even be visible.

The "proton-tagging" technique [28, 29] is a coincidence method which takes advantage of the fact that protons are easier to detect than neutrons. In that technique quasi-elastic electron scattering is measured with an additional charged-particle detector centered around the direction of the momentum-transfer vector, $\vec{q}$. If no proton is detected, the event is ascribed to scattering from the

neutron. This technique generally requires theory-based corrections to account for the tail of the Fermi-motion which would cause a recoil proton to miss the charged-particle detector (or cause a spectator proton to hit it).

We propose to use the "ratio-method" [38] which is discussed in detail in the next section. It relies on measurement of both the recoil protons and recoil neutrons [30–37]. If the particle detection, particularly the neutron detection is well understood, this technique is subject to the smallest systematic errors.

There are relatively few measurements of G_M^n beyond $Q^2 = 1$ $(GeV/c)^2$. The few published measurements in the range $1 < Q^2 < 4.5$ $(GeV/c)^2$ (shown in Fig. 1) have been eclipsed, both in number of points and in precision, by the recent CLAS data [37,39] of Lachniet. These (not yet published) data are shown in Fig. 1 as the blue points. Several of the proposers of the present experiment played key roles in the CLAS experiment. The ratio-method was used for those measurements and will be used in the proposed experiment.

In the figure, the value of G_M^n is divided by the 'scaled dipole'. The dipole is vector-meson-dominance-inspired empirical parameterization of the proton's electric form factor: $G_E^p \approx G_D = (1 + Q^2/.71 \ (GeV/c)^2)^{-2}$. This appeared to be a good approximation for G_E^p over a large Q^2 range until recent recoil-polarization measurements [2,3]) showed that G_E^p actually fell rapidly below the dipole form for $Q^2 > 1$ $(GeV/c)^2$. The scaling approximation hypothesizes that $G_M^p \approx \mu_p G_D$ and $G_M^n \approx \mu_n G_D$. The CLAS data show that the 'scaled dipole' is a surprisingly good approximation for G_M^n out to $Q^2 \approx 4.5$ $(GeV/c)^2$.

Beyond $Q^2 = 4.5$ $(GeV/c)^2$ there are only a few points, with large errors. The points plotted in green in Fig. 1 are SLAC measurements [26] made using the "proton-subtraction" technique. While these points have relatively large errors, they point to a trend which is not seen in the CLAS data. This makes it particularly interesting to investigate the behavior of G_M^n in the range $3.5 < Q^2 < 8$ $(GeV/c)^2$ with a measurement which is independent of either of those shown in Fig. 1. (A similar plot is presented at the end of the proposal, with the projected errors of the proposed measurement superimposed.)

With the technique proposed here, it is possible to obtain high-precision measurements of G_M^n over that Q^2 range using the beam which is *presently available* at JLab.

2   Technique

We propose to use the "ratio method" [38] to determine G_M^n from quasi-elastic electron scattering on the deuteron for $3.5 < Q^2 < 8$ $(GeV/c)^2$. This method is far less sensitive to systematic errors than the "proton-subtraction" or "proton-tagging" techniques.

Use of the "ratio method" requires the measurement of both neutron-tagged, d(e,e'n), and proton-tagged, d(e,e'p), quasi-elastic scattering from the deuteron. Simultaneous measurements of both these reactions provides a substantial reduction of systematic error because the detection efficiency for the scattered electron then cancels in forming the ratio:

$$R'' = \frac{\frac{d\sigma}{d\Omega}\big|_{d(e,e'n)}}{\frac{d\sigma}{d\Omega}\big|_{d(e,e'p)}} \tag{1}$$

With a small ($\approx 1\%$) calculable nuclear correction, ϵ_{nuc}, this measured ratio of quasi-elastic cross
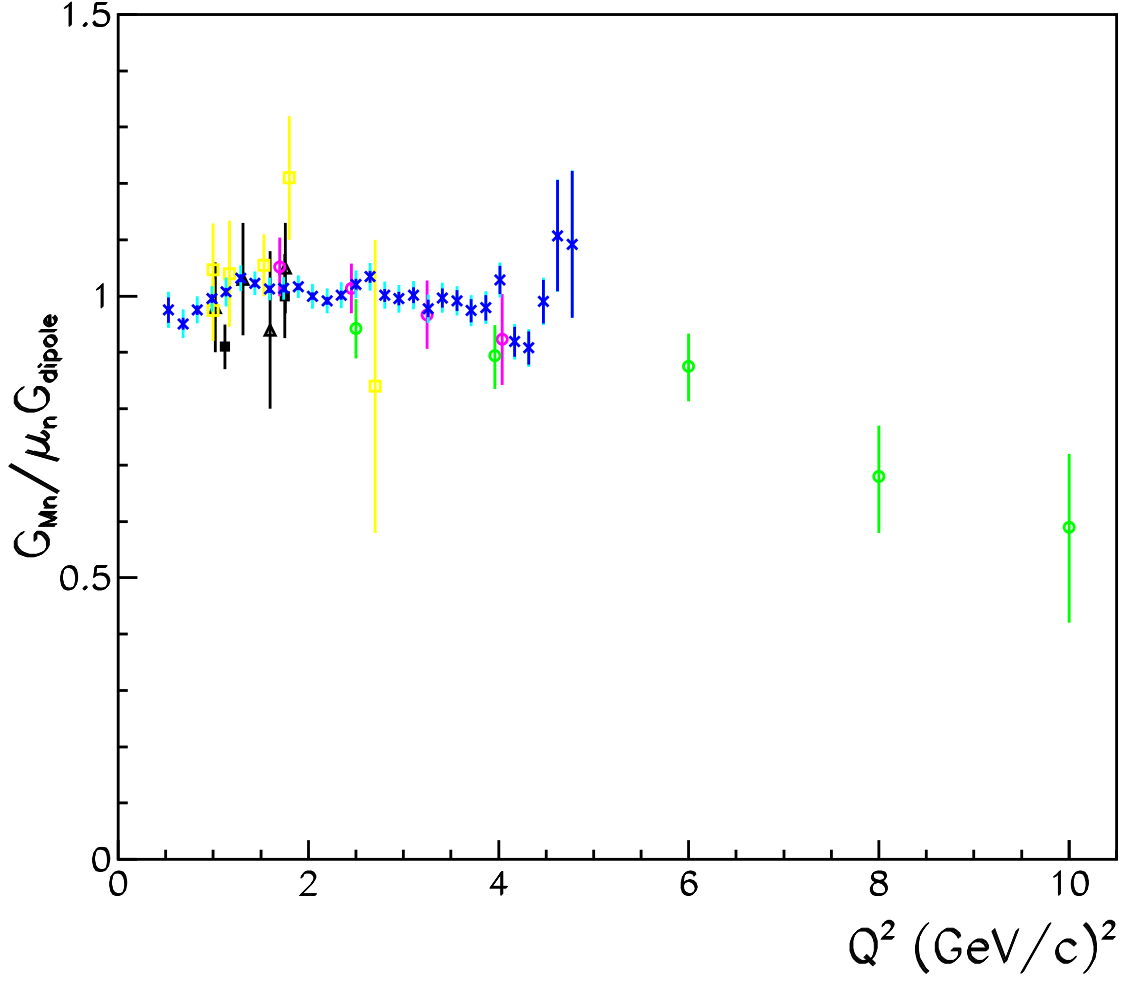
Figure 1: Existing data on G_M^n in $Q^2 > 1$ (GeV/c)^2 range are plotted as ratio to scaled dipole approximation. Blue points are from CLAS e5 run [37, 39]. Dark lines show the statistical error while light lines are the quadrature sum of statistical and systematic errors. Green circle [26] and magenta circle [27] points are from SLAC. Older data are shown as yellow squared [31], solid squares [29], and hollow triangles [25]. Some points have been slightly displaced horizontally to avoid overlap.

sections can be used to determine the ratio of the elastic cross sections:

$$R' = \frac{R''}{1 + \epsilon_{\text{nuc}}} = \frac{\frac{d\sigma}{d\Omega}\big|_{\text{n(e,e')}}}{\frac{d\sigma}{d\Omega}\big|_{\text{p(e,e')}}} = \frac{\eta\frac{\sigma_{\text{Mott}}}{1+\tau}\left((G_E^n)^2 + \frac{\tau}{\epsilon}(G_M^n)^2\right)}{\frac{d\sigma}{d\Omega}\big|_{\text{p(e,e')}}}$$

where, as above,

$\eta = \frac{1}{1 + 2\frac{E}{M_N}\sin^2(\theta/2)}$

$\epsilon^{-1} = 1 + \vec{q}^2/Q^2\tan^2(\theta/2) = 1 + 2(1+\tau)\tan^2(\theta/2)$

and $\tau = Q^2/4M_N^2$

Then, with a minor correction (≈ 1 %, using the Galster parameterization) for the electric form factor of the neutron, this in turn allows determination of the ratio of interest,

$$R = R' - \frac{\eta\frac{\sigma_{\text{Mott}}}{1+\tau}(G_E^n)^2}{\frac{d\sigma}{d\Omega}\big|_{\text{p(e,e')}}} = \frac{\eta\sigma_{\text{Mott}}\frac{\tau/\epsilon}{1+\tau}(G_M^n)^2}{\frac{d\sigma}{d\Omega}\big|_{\text{p(e,e')}}} \tag{2}$$

This measurement of R then allows G_M^n to be determined, given just the proton's elastic cross-section at the corresponding kinematics.

It may be noted that, because R is proportional to the square of G_M^n, the fractional error on G_M^n will actually be only half of the fractional error on R. Since the quantity of greatest interest is G_M^n, it is conventional to report the expected size of the errors on G_M^n. However, the experiment will actually be a direct measurement of R'' (from which R is inferred with small corrections). This distinction is significant only in that present uncertainties on the proton's form factors (and cross section) do not actually imply systematic errors on the quantity being measured, R'' (or R). Subsequent improvements in the determination of the proton cross section, at the kinematics of interest, can be combined retrospectively with the results for R from this measurement to obtain improved values for G_M^n. There would be no need to repeat the analysis of this experiment to incorporate new proton measurements.

3   Proposed Kinematics

The kinematic points at which we propose to measure are shown in Table 1. The lowest Q^2 points will overlap with existing CLAS measurements while the highest Q^2 points will greatly extend the range in which G_M^n is known with high precision

While the scattered electron energy is relatively constant (near 2 GeV) across the kinematic points, the central nucleon momentum of interest is seen to vary from 2.65 GeV/c to 5.1 GeV/c. Individual calibrations with 'tagged' protons and 'tagged' neutrons will be carried out at four of the kinematic points to ensure that the neutron and proton detection efficiencies are well known.

4   Apparatus

The use of the ratio method depends upon detection of both scattered neutrons and protons. Potential sources of systematic error arise in determining the acceptance and detection efficiency of these particles. Errors associated with nucleon acceptance can be reduced by matching the neutron and proton acceptances so they cancel in the ratio (as does the electron acceptance and efficiency).

Table 1: Kinematics of proposed measurements

Q^2 (GeV/c)^2	E_{beam} (GeV)	θ_e	θ_N	E' (GeV)	P_N (GeV/c)
3.5	4	37.5°	28.7°	2.1	2.65
4.5	4	49.5°	21.7°	1.6	3.2
5 25	5	40.4°	22.7°	2.3	3.6
6	5	48.1°	18.7°	1.8	4.0
7	6	42.0°	18.7°	2.3	4.6
8	6	52.0°	14.9°	1.7	5.1

We propose to use the existing BigBite spectrometer in Hall A to measure the momentum and angle of the scattered electrons and the BigHAND detector to detect both the scattered neutrons and protons. Nucleons scattered toward the BigHAND detector will pass through the field of a large aperture dipole magnet which will be positioned along the nucleon flight path to vertically deflect protons relative to neutrons. The layout of the experiment is shown schematically in Fig. 2.

The targets will be 10 cm long liquid deuterium (and liquid hydrogen for calibration) cells with 100 μm aluminum windows. This gives about 1.7 g/cm^2 of target compared to about 0.054 g/cm^2 in the windows. As discussed below, selection cuts will reduce the contribution of quasi-elastic events from aluminum below this 3.2% ratio. To obtain percent-level precision, however, it will be necessary to subtract the contribution from the windows. A dummy target cell will be used, having windows at the same position as the real cell but with windows thick enough to give the same luminosity as for a full cell. Sufficient statistics for subtraction of the windows will be obtained by running on the dummy cell for about four percent of the beam time used for the full target.

As discussed below, past experience suggests the BigBite and BigHAND detector rates will be reasonable at a luminosity of 10^{37}/A where A is the number of nucleons in the target. For a luminosity of 0.5×10^{37} on a 10 cm deuterium target, the beam current would be about 2 μA.

BigBite, shown in Fig. 3, is a large acceptance non-focusing magnetic spectrometer. It has a large acceptance (roughly 44 mSr in the intended configuration) and has been used successfully at high luminosity ($\approx 10^{37}$/cm^2/s). It will be configured for high momentum measurements, with the entrance aperture of the dipole 1.55 m from the target and the drift chambers separated by 1.4 m. In this configuration, the expected momentum resolution will be $\sigma p/p \approx 0.5$ to 0.6% (found by scaling from the 1% resolution obtained in the GEn [40, 41] experiment for 3.2 GeV/c electrons to the momenta of interest here, 1.6 to 2.1 GeV/c, and accounting for the higher bend-plane resolution resulting from doubling of the chamber spacing). The angular resolution is expected to be better than 1 mr in both horizontal and vertical angles [42].

The addition of a gas Cerenkov detector in BigBite is expected to eliminate the majority of the trigger rate which was seen in the GEn experiment. Analysis of that data showed that most BigBite triggers were not associated with any charged tracks, indicating that the shower counters had been triggered by high energy photons from π^0 decay. Elimination of this source of false triggers is expected to reduce the trigger rate in BigBite to a few hundred Hz. Therefore we intend to run using just BigBite (with the gas Cerenkov required) as a trigger.

The BigHAND (Hall A Nucleon Detector), shown in Fig. 4, is a large array of scintillators

BigBen
proton deflector

17m TOF

BigHAND
nucleon detector
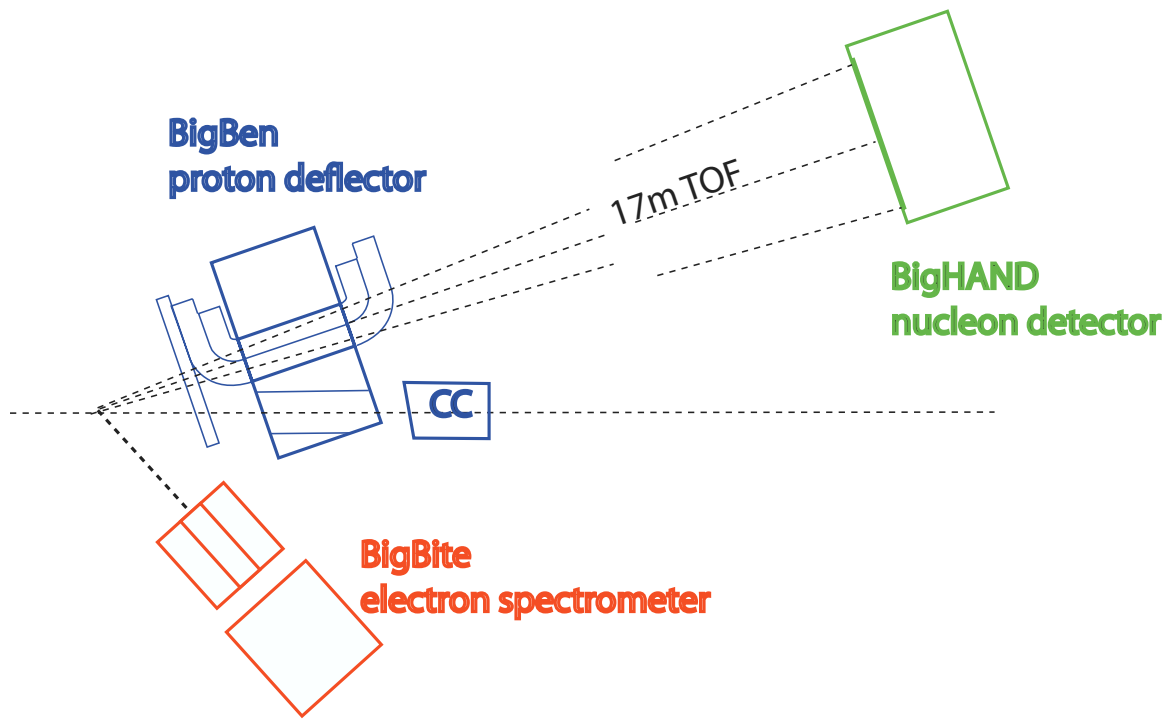
CC

BigBite
electron spectrometer

Figure 2: A schematic view of the apparatus is shown. BigBite will detect scattered electrons while BigHAND will detect the scattered nucleons. The dipole magnet "BigBen" will deflect protons for the purpose of particle identification. Note: the 17 m flight path to BigHAND is not drawn to scale.
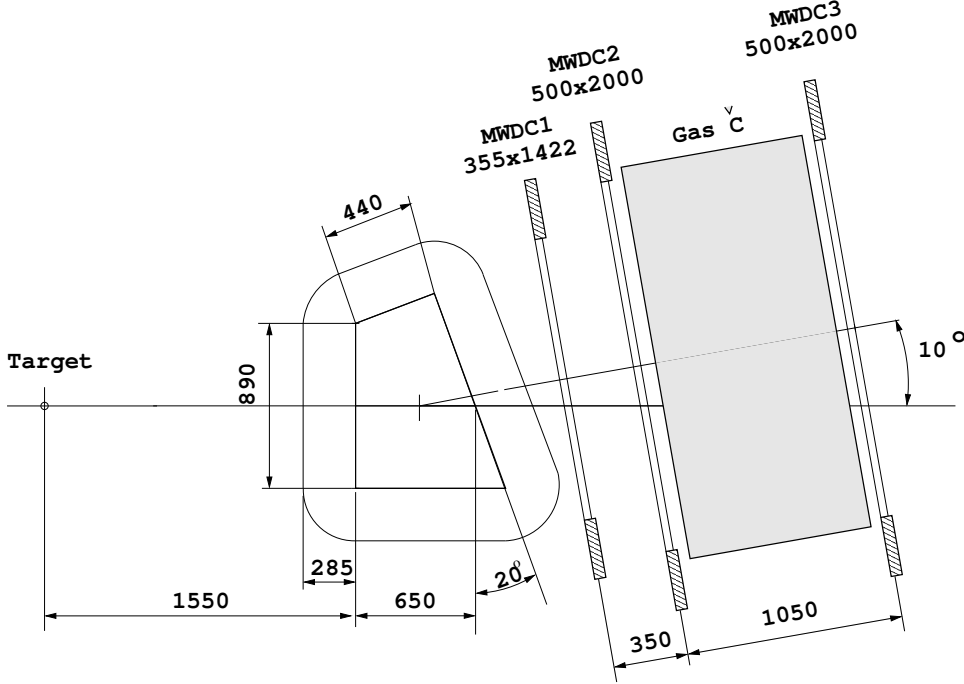
Figure 3: The BigBite spectrometer, configured for high momentum running. The wire chamber separation is increased to 1.4 m and a gas Cerenkov counter is located between the last two chamber packages.

interspersed with seven half-inch thick iron converters which initiate hadronic showers. A "veto" layer on the front face was intended to distinguish neutrons from protons. (An alternative technique will be employed for this measurement, as will be discussed below.) Heavy shielding (2 inches of lead and 1 inch of iron) reduces the electromagnetic rate in the scintillators. The observed r.m.s. spatial resolution of reconstructed hadronic showers for the GEn experiment [40] is typically 4.3 cm. vertically and 7 cm. horizontally. The detector will be located 17 meters from the target so the corresponding angular resolution will be 2.5 mr and 4 mr (0.15° and .24°), respectively. With the higher nucleon momentum of the present proposal, the resolution may be be somewhat improved, especially in the horizontal direction.

The r.m.s. time-of-flight resolution of the overall detector array is approximately 400 ps [43]. With a 17 meter flight path, there will be at least 0.95 ns of time difference between a prompt particle (photon or charged pion) and even the highest energy neutrons of interest (see Table 2). This will enhance the rejection of photons (which are largely attenuated by the existing shielding).

The efficiency predicted by simulation [44] for conversion and detection of neutrons and protons in the momentum range of interest is shown in Fig. 5 for a 20 MeV (electron equivalent) threshold. For neutrons, the predicted efficiency is seen to be over 70% at the lowest Q^2 of interest and to rise to over 90% at the highest Q^2. The proton efficiencies are even higher. If neutron/proton identification were based solely upon the response of the 'veto' layer, then contamination by mis-identification would be a significant problem. Experience from the GEn experiment [40] indicates that about 2.5% of (independently identified) protons fail to fire the veto layer and would be mis-identified as neutrons [41]. More troublesome is the fact that a significant fraction ($\approx 40\%$) of the detected neutrons actually fire the veto layer (because the hadronic shower is initiated in the front shielding).
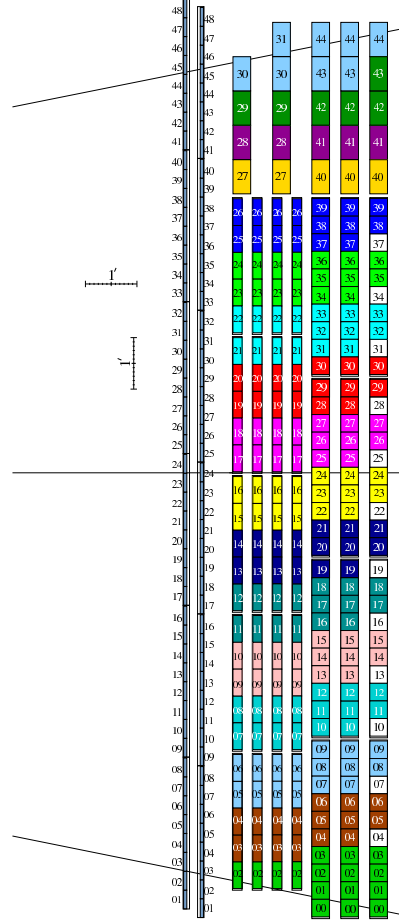
Figure 4: The BigHAND (Hall A Nucleon Detector). Iron converters initiate hadronic showers which are detected by the large scintillators.

Table 2: Flight time for nucleon vs. photon for 17 m flight path

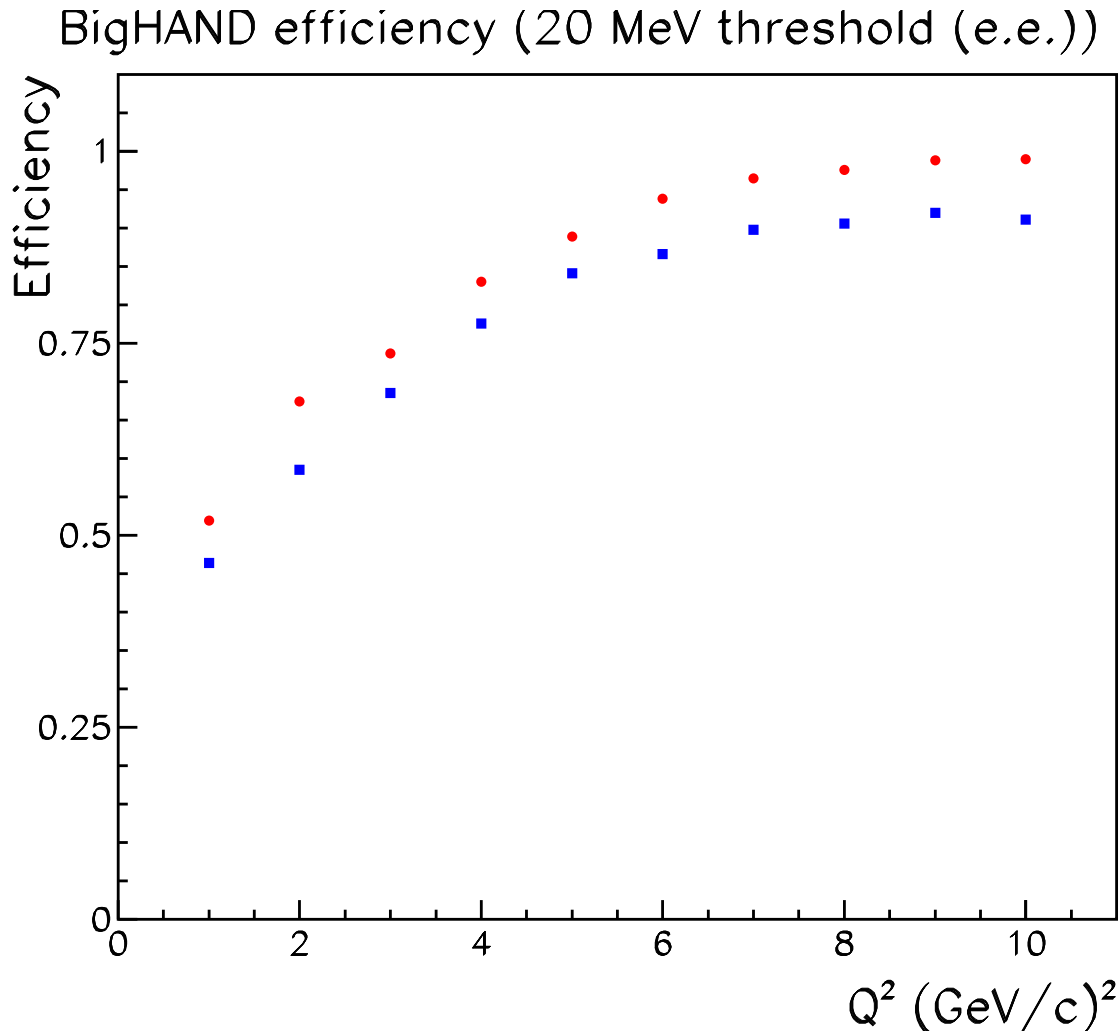| Q^2 (GeV/c)^2	θ_N	P_N (GeV/c)	T_N (ns)	$T_N - T_\gamma$ (ns)
3.5	28.7°	2.65	60.1	3.4
4.5	21.7°	3.2	59.0	2.4
5.25	22.7°	3.6	58.7	2.0
6	18.7°	4.0	58.2	1.54
7	18.7°	4.6	57.8	1.17
8	14.9°	5.1	57.6	0.95

Figure 5: The predicted [44] detection efficiency of BigHAND is shown for neutrons (blue squares) and protons (red circles) as a function of the central nucleon momentum associated with each Q^2.

Event topology could be used to more cleanly identify a subset of more unambiguous neutrons or protons but at the cost of a large reduction in detection efficiency.

A much more clean separation of neutrons from protons can be made, without loss of efficiency, by introducing a dipole magnet to deflect the protons vertically upwards. If the initial direction of the nucleon could be accurately predicted, then only a small deflection would be needed to distinguish charged particles from neutral ones. In the the case of quasi-elastic scattering, the measured $\vec{q}$-vector does not precisely predict the direction of the struck nucleon's final momentum since the initial momentum of the nucleon within the deuteron also contributes. Using a reasonable model of the deuteron's wave-function [46], the momentum distribution can be determined. It is found that, with 95% probability, the component of the nucleon's momentum along any chosen direction is less than 100 MeV/c. A magnetic 'kick' of 200 MeV/c, then would separate quasi-elastic protons from neutrons at the 95% level. In the simplest analysis, a horizontal line could be defined across the face of BigHAND (for any given event detected in BigBite) such that the struck

nucleon would have a 95% probability of falling below the line if the particle were a neutron and a 95% probability of falling above the line if the particle were a proton.

The remaining 5% mis-identification can still be accurately corrected by using the 'veto' layer (and possibly event topology) to determine the actual distribution of neutron and proton events relative to the ideal positions they would have for elastic kinematics. In particular the spread of the neutron distribution relative to the $\vec{q}$-vector can be investigated by studying the sample which do not fire the veto (and making a modest correction for protons). Also, since the initial momenta of the nucleons are vertically symmetric, the actual distributions of neutron and proton events can be empirically determined by observing the distributions of those neutrons which are displaced downward from the point predicted for elastic kinematics and those protons which are displaced upwards from the (magnetically deflected) point predicted for elastic kinematics. Either of these correction techniques should allow the systematic errors due to neutron/proton mis-identification to be reduced to well below 1%, and the comparison of the two techniques should allow the confident determination of this contribution to systematic error.

The 200 MeV/c kick required to separate quasi-elastic protons from neutrons can be achieved by applying a dipole field, near the beginning of the flight path, having a field integral of $\int Bdl \approx 0.7$ T·m. We have identified a large-aperture magnet at Brookhaven National Laboratory which could be used for this purpose. In its present configuration, this "48D48" magnet, shown in Fig. 6 has a 120 cm × 120 cm (48 in. × 48 in.) pole face with a 50 cm gap.

The magnet would be modified so it can be positioned near the beam line. This would involve machining a hole through the return yoke to provide a low-field, iron-free region for passage of the outgoing beam. Asymmetric field coils would also be needed to avoid interfering with the outgoing beam, One possible solution, shown in Fig. 2, involves the use of an existing standard-coil/booster-coil pair originally designed to drive half of a 100 cm gap magnet. Correcting coils would be used to compensate for beam steering due to any residual fields.

The details of the yoke hole, field coils, field clamps, and correcting coils will be finalized using a magnetic field simulation program such as TOSCA. The magnet modifications will be designed such that the magnet can also be used for the recently-approved high-Q^2 proton elastic cross section experiment [47].

5 Acceptance and Fiducial Cuts

Here we discuss event-selection cuts which will be applied to reduce systematic errors due to acceptance losses.

In the case of elastic kinematics (applicable for the calibration reactions discussed in the next section) there is a direct mapping of scattered-electron direction to recoiling-nucleon direction. The acceptance of both BigBite and BigHAND can be conveniently expressed in terms of the electron-scattering angles. The solid angle for acceptance of coincidence events is then found from the overlap of the acceptance of the two detector systems. This is shown, for four kinematic points, in Fig. 7 with the full geometric acceptance of BigBite and a reduced acceptance of BigHAND, as discussed below.

For quasi-elastic events, the $\vec{q}$-vector can be reconstructed based on the scattered-electron momentum and direction measured by BigBite, A fiducial cut can be placed on the direction of $\vec{q}$ to choose the central direction of the scattered nucleons. While Fermi motion will widen the image,

Figure 6: Assembly diagram for generic 48D48 spectrometer magnet. Magnet is shown mounted for horizontal bend-plane but will be used for vertical bend plane. Coil configuration shown is that used at BNL.
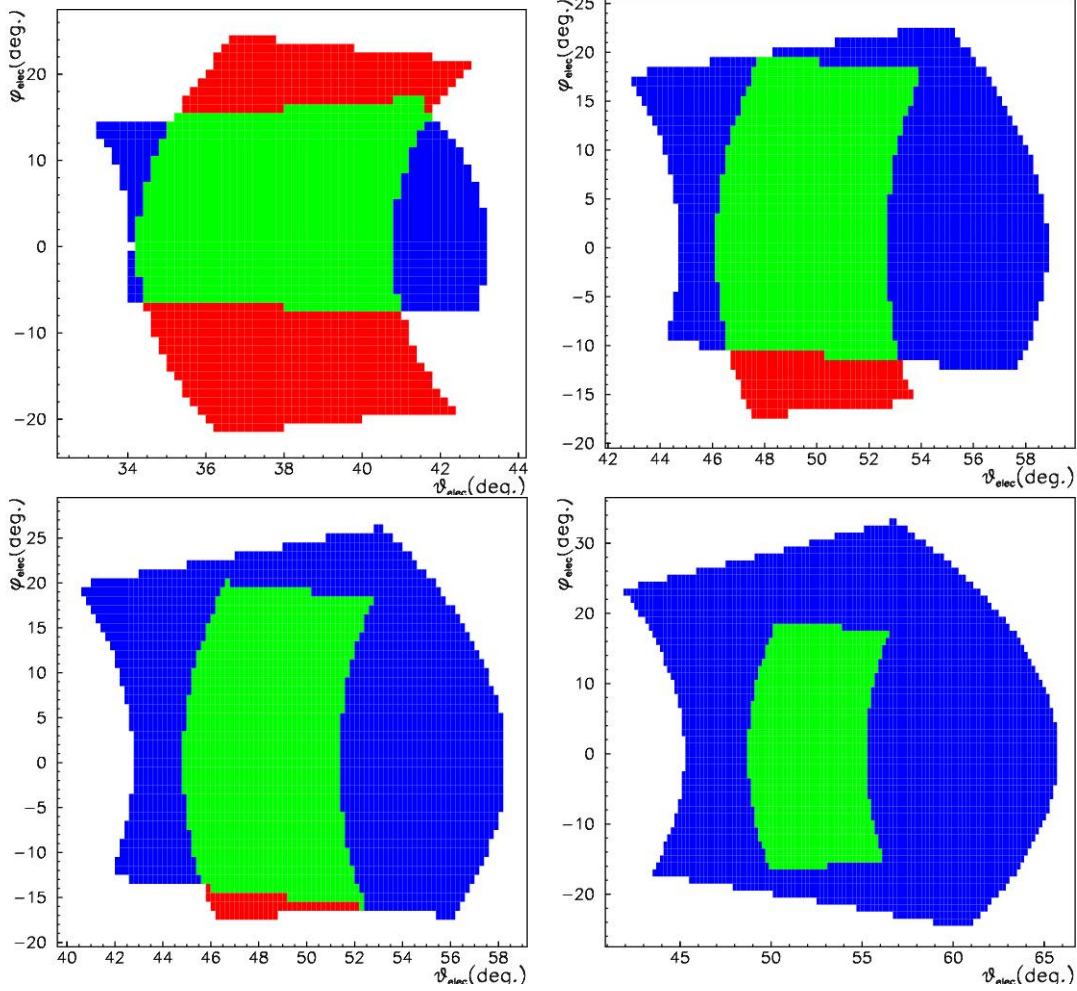
Figure 7: The acceptance of BigBite as a function of electron scattering angles (θ, ϕ) is shown in red in each figure, the acceptance of BigHAND for elastically scattered nucleons *as a function of the electron scattering angles* is shown in blue. The overlap (corresponding to coincident acceptance for elastic events) is shown in green. The acceptance of BigHAND used for the plot is a subset for which an elastic proton or neutron would both fall in the active area. The four plots correspond to four kinematic points (see Table 1): Upper left, $Q^2 = 3.5$, upper right, $Q^2 = 4.5$, lower left, $Q^2 = 6.0$, lower right, $Q^2 = 8.0$ (GeV/c)^2

the ideal case of elastic scattering can be used to map the acceptance to a position distribution of neutrons on BigHAND (and a similar proton distribution, taking into account the shift caused by the deflection of the dipole magnet). The green overlap regions in Fig. 7 represent the angular region of the BigBite acceptance for which scattering at elastic kinematics would send a nucleon into the BigHAND acceptance regardless whether it was a neutron or proton. Potential systematic errors are greatly reduced by *using the same fiducial region for both neutron-coincident and proton-coincident measurements*. The 'image' of the fiducial region projected onto BigHAND will differ for protons and neutrons because of the vertical kick given to the protons by the dipole magnet. To first order, the effect of this offset can be prevented from introducing a difference in acceptance by using a reduced fiducial region. The fiducial is defined so neutrons scattered in the $\vec{q}$ direction would not occupy a strip at the top of BigHAND. The size of this strip is chosen so that the shift in the proton image relative to the neutron image does not deflect the protons out of the BigHAND acceptance. Rather, it causes the elastic protons to occupy the top of BigHAND, leaving a similar unoccupied strip at the bottom of BigHAND. The size of the strip is set by the $\Delta p = 200$ MeV/c transverse kick given given to the protons by the dipole, the nucleon momentum, p_N, and the distance, L from the target to BigHAND. While quasi-elastic protons (and neutrons) are not guaranteed to remain within the acceptance, the matching of the acceptance losses is improved by this reduced fiducial cut. Reducing the size of BigHAND by this strip of size $D = \frac{\Delta p}{p_N} L$ at the top when calculating the elastic neutron acceptance gives the BigHAND coverage shown in Fig. 7 and the resulting fiducial region shown.

A further refinement will be used for the three lowest-Q^2 kinematic points, to reduce systematics. For the Q^2=3.5 (GeV/c)^2 point, the combined elastic acceptance would be largely determined by BigHAND if the full BigBite acceptance shown in Fig. 7 were used. So elastic events selected by such a fiducial would have scattered nucleons extending to the edge of the BigHAND acceptance. With the addition of Fermi motion, the quasi-elastic events may be expected to have a larger loss, by falling outside the BigHAND acceptance, than would be the case at the other kinematic points. Monte Carlo simulation (described in section 7.1) confirms that the acceptance losses are larger at this kinematics, amounting to 13.5% (see top P_{coinc} value in Table 3). To the extent that the acceptance losses are equal for protons and neutrons, they cancel in the ratio R'' (Eqn. 1). Systematic errors may arise, however, due to difference in the acceptance-corrections resulting from effects such as horizontal steering by the dipole's field, multiple-scattering, or edge effects in nucleon detection efficiency. It is therefore prudent to reduce the acceptance corrections where practical. This can be effected by choosing a new smaller fiducial, based on BigBite measurements, by demanding that the $\vec{q}$ vector point towards a further-reduced portion of the BigHAND face. A margin of safety, d, is excluded around all edges. (This adds to D, introduced earlier, at the top of the detector for neutrons and at the bottom of the detector for protons). This is represented graphically in Fig. 8 which shows the BigBite acceptance (in local coordinates) and superimposed images of the trajectories which would give elastic events at the edge of BigHAND (green) or at the edge of such a safety margin(red). If d is chosen as $d = \frac{\delta}{p_N} L$ then, to first order, quasi-elastic coincidences with the electron within the fiducial cut will be lost only if the struck nucleon had a component of momentum of at least δ directed towards the edge of BigHAND. Table 3 gives the resulting fractional acceptance, P_{coinc}, in BigHAND for various choice of δ. The cost of applying this tighter fiducial cut is a smaller fractional acceptance for quasi-elastically scattered electrons, also summarized in Table 3. The rate calculations in this proposal are based upon fiducial cuts corresponding to $\delta = 80$ MeV/c for Q^2 =3.5 (GeV/c)^2 and $\delta = 40$ MeV/c for the two points at

Table 3: Top rows give the fraction, f_{fid}, of quasi-elastic electrons in BigBite which pass the fiducial cut. Bottom rows give calculated probability, P_{coinc} for a quasi-elastic electron which passes the fiducial cut, that the corresponding nucleon will fall within the BigHAND active area. For the lowest Q^2 kinematic points, results for several fiducial cuts are presented with 'safety margin' set by δ. For convenience, lower rows also give $\mathcal{F}_{\text{acc}}(\delta) = f_{\text{fid}}(\delta)/f_{\text{fid}}(0)$, the fraction of events surviving a cut given by δ.

$Q^2 =$	3.5		4.5		6.0	8.0$(\text{GeV/c})^2$	$\delta(\text{MeV/c})$
$f_{\text{fid}}(\%)$			$f_{\text{fid}}(\%)$		$f_{\text{fid}}(\%)$	$f_{\text{fid}}(\%)$	
67.2			78.0		87.8	98.8	0
59.9			74.0				20
50.2			68.6				40
39.4			61.7				60
28.5			52.3				80
17.7			41.0				100
8.1			28.9				120
$P_{\text{coinc}}(\%)$	$\mathcal{F}_{\text{acc}}(\delta)(\%)$		$P_{\text{coinc}}(\%)$	$\mathcal{F}_{\text{acc}}(\delta)(\%)$	$P_{\text{coinc}}(\%)$	$P_{\text{coinc}}(\%)$	
86.5	100		93.0	100	95.5	97.5	0
90.4	89.		94.1	95.			20
92.9	75.		95.3	88.			40
94.7	59.		96.4	79.			60
96.0	42.		97.1	67.			80
96.5	27.		98.1	53.			100
97.0	12.		98.4	37.			120

Table 4: Combined acceptance of BigBite and BigHAND for elastic events and for quasi-elastic events with fiducial cut. The quantities f_1 and f_2 are defined in the text.

Q^2 (GeV/c)^2	3.5	4.5	6.0	8.0
$\Delta\Omega_{el}$ (mSr)	39.6	53.6	53.6	53.2
f_1 (%)	78.6	87.2	92.0	96.3
f_2 (%)	28.5	65.7	87.8	98.8
$\Delta\Omega_{eff} = f_1 f_2 \Delta\Omega_{el}$ (mSr)	8.86	32.1	43.1	50.6
P_{coinc} (%)	96.0	95.3	95.5	97.5

$Q^2 =$4.5 and $5.25(\text{GeV/c})^2$. With these cuts, the estimated loss of acceptance due to Fermi motion will be less than 5% at all kinematic points. This limits the potential for systematic errors due to the difference in the loss of protons compared to neutrons. The cost of these cuts is a reduction by 58% in the counting rate at the lowest Q^2 point, 12% at $Q^2 =$4.5 (GeV/c)^2 and 13.5% at $Q^2 =$5.25 (GeV/c)^2. Since the count rates are relatively high at these kinematic points, the loss of acceptance is justified by the decreased sensitivity to systematic error.

Table 4 gives the combined solid angle $\Delta\Omega$ of BigBite and BigHAND for elastic events at several kinematic points. Also given (based on the quasi-elastic Monte Carlo described in section 7.1) are f_1, the fraction of events for which the electron and nucleon still fall into the combined acceptance once Fermi motion is included and f_2, the fraction of those events which would pass the fiducial cut. The product $f_1 f_2 \Delta\Omega$ can be treated as an effective solid angle for accepting quasi-elastic events with the fiducial cut. This is intended only to give an estimate of the size of these separate effects. In final rate estimates, these effects are not treated as separate factors but are included event-by-event in the Monte Carlo integration of cross section over acceptance. For convenience, the last line of Table 4 summarizes the motivation for the fiducial cuts by giving the the fraction, P_{coinc}, of quasi-elastic events within the fiducial cut for which the scattered nucleon also falls within the BigHAND acceptance. The resulting acceptance fraction P_{coinc} are seen to be near unity and are expected to be nearly equal for neutrons and protons. (P_{coinc} is also given in Table 3 but here it is given for the selected fiducial cuts.)

6   Nucleon Detection Efficiency Calibration

While the efficiency of electron-detection cancels in the ratio, R''(equation 1), that is not true for the neutron or proton detection efficiencies. The efficiency of BigHAND's detection of these particles could be calculated in Monte Carlo, as has been done for lower energies [44], but a reliable determination of the efficiency at the percent level will require calibration with tagged sources of known protons and neutrons. Fortunately the efficiency may be expected to be quite stable since it is largely determined by the mass distribution in the detector and the resulting probability of hadronic shower initiation. Factors, such as gain, threshold, and light yield have a relatively minor effect since most showers produce large numbers of secondaries and so their total light output is well above threshold. This stability is demonstrated in Fig. 9 which shows the *ratio* of the efficiency found [44] for a threshold of 20 MeV (electron equivalent) to that found with a threshold of only 5
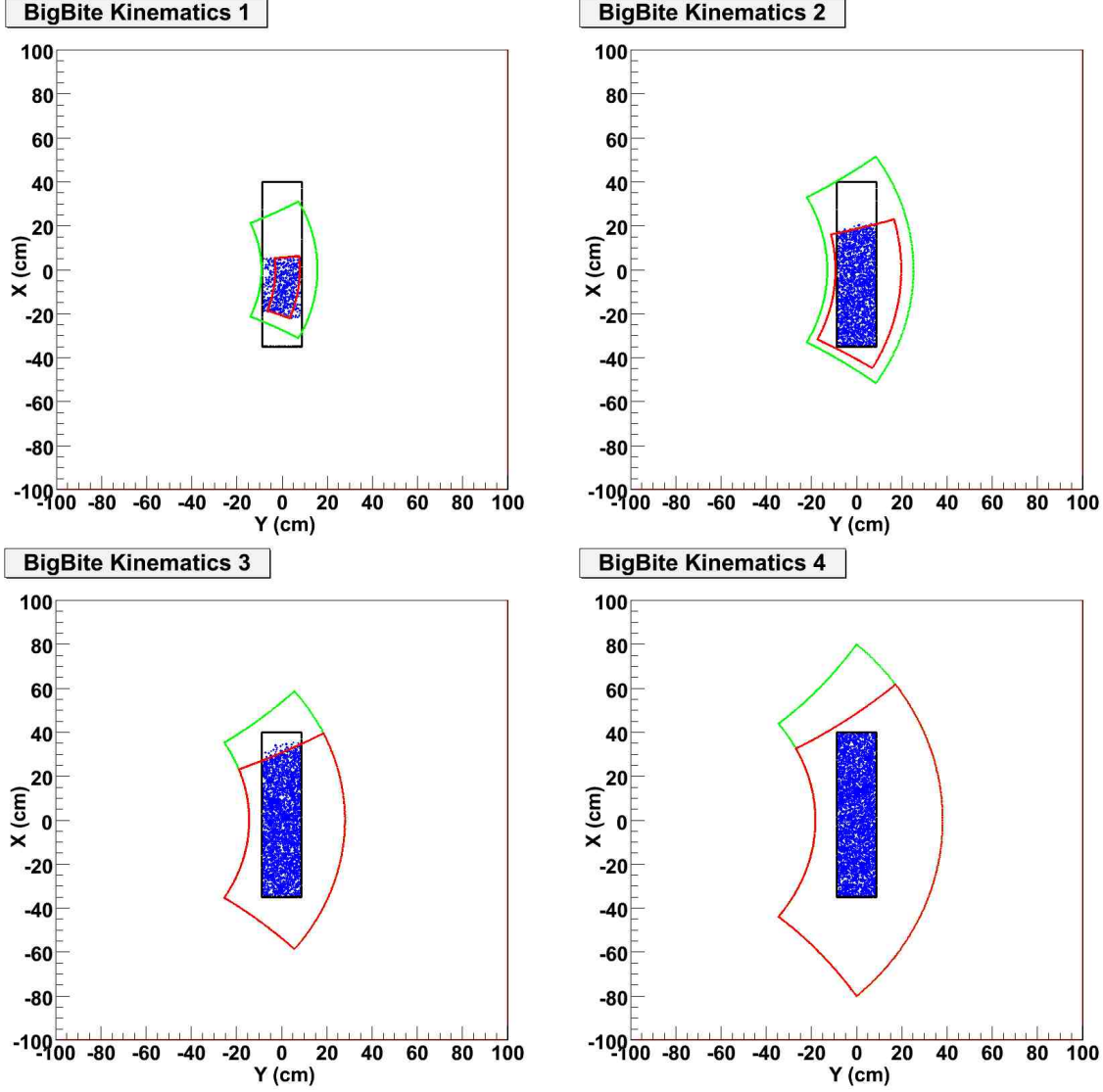
Figure 8: The acceptance of BigBite (rectangle) in terms of the horizontal (y) and vertical (x) position of a track at the entrance. Also shown is the locus of elastically scattered electrons which would result in a nucleon a) at the edge of the BigHAND acceptance (green) and b) at the edge of the reduced acceptance corresponding to a safety margin at the edge of BigHAND (red). The part of the BigBite acceptance within this region corresponds to the fiducial cut for elastic kinematics. Dots show position at entrance of BigBite for simulated quasi-elastic electrons which satisfy the fiducial cut. The four plots correspond to four kinematic points (see Table 1): Upper left, $Q^2 = 3.5$, upper right, $Q^2 = 4.5$, lower left, $Q^2 = 6.0$, lower right, $Q^2 = 8.0$ (GeV/c)^2

MeV (electron equivalent). Even at the lowest Q^2 of interest, 3.5 $(\text{GeV/c})^2$, such a huge change in threshold would result in only $\approx 10\%$ change in efficiency. This is in contrast to detection of low energy neutrons in scintillator, for which the detection efficiency is a strong function of effective threshold. Furthermore, since BigHAND's detection is based purely on scintillation, it is immune to the rapid changes in efficiency and background which can more typically occur in wire chambers. Because the efficiency will be stable, it is sufficient to have separate calibration runs, rather than simultaneously taking calibration data by having the calibration target in place along with the deuterium target.

For both protons and neutrons, the basis of the calibrations is a cleanly identified reaction on the proton which produces a 'tagged' nucleon with a known momentum vector, (p(e,e')p for proton calibration and p(γ,π^+)n for neutron calibration). BigHAND is then searched for the nucleon near the expected position and the detection efficiency is determined as the ratio of the number of tagged events for which the nucleon is found to the total number of tagged events.

6.1 BigHAND Calibration Coverage

The $p(e, e'p)$ proton-calibration reaction and the $p(\gamma, \pi^+ n)$ neutron calibration reaction have essentially the same (elastic-scattering) kinematics. A disadvantage of the use of elastic kinematics for calibration is that the acceptance of BigBite for electrons maps into a well-defined corresponding angular range on the BigHAND detector face (see Fig. 10). Regions beyond that, which would not be illuminated by calibration particles, may still be of interest for quasi-elastic events since the particles are then smeared beyond the strict elastic kinematic boundaries by the nucleon's initial momentum. To reduce the impact of the larger 'footprint' of quasi-elastic events, calibration data will be taken at two positions of the BigBite spectrometer so the face of BigHAND will be more widely illuminated by calibration nucleons. This expanded calibration region is illustrated in Fig. 11 which also shows the distribution of quasi-elastic nucleons coincident with electrons within the fiducial region selected by BigBite. (The simulation is described in section 7.1.) Table 5 shows the predicted fraction of quasi-elastic coincidence events for which the detected nucleon will fall inside this calibration region. As described below, extrapolation of lower-momentum calibration data will also be used to estimate efficiencies for those events which are outside the elastic-calibration region at the momentum of interest. Calibration measurements will be made only at the four kinematic points shown in Fig. 11 and listed in Table 5. For the other two kinematic points, $Q^2 = 5.25$ and 7.0 $(\text{GeV/c})^2$, the efficiency will be interpolated from measurements made at lower and higher Q^2. This results in a significant savings of beam time (and setup time for spectrometer moves and polarity-reversals) at a cost of increased systematic errors on these two 'fill-in' points. The more complete kinematic coverage resulting from including these points, even with larger systematic errors, justifies the beam time needed to take the measurements. Furthermore, the systematic errors due to the interpolation of the nucleon detection efficiencies can be conservatively estimated to be under 2%. The hadronic cross sections change quite slowly in the region in which these interpolations will be made (the magenta arrows in Fig.12), as a result of which the estimated efficiencies shown in Fig. 5 change only moderately in the regions of interest (interpolating to $Q^2 = 5.25$ $(\text{GeV/c})^2$ from the points at 4.5 and 6 and interpolating to $Q^2 = 7$ $(\text{GeV/c})^2$ from the points at 6 and 8.) The method of interpolation is described in the next paragraph.

Those regions of BigHAND which are not directly calibrated at a particular nucleon momentum will be illuminated by the lower momentum calibration nucleons at other kinematic points. In this
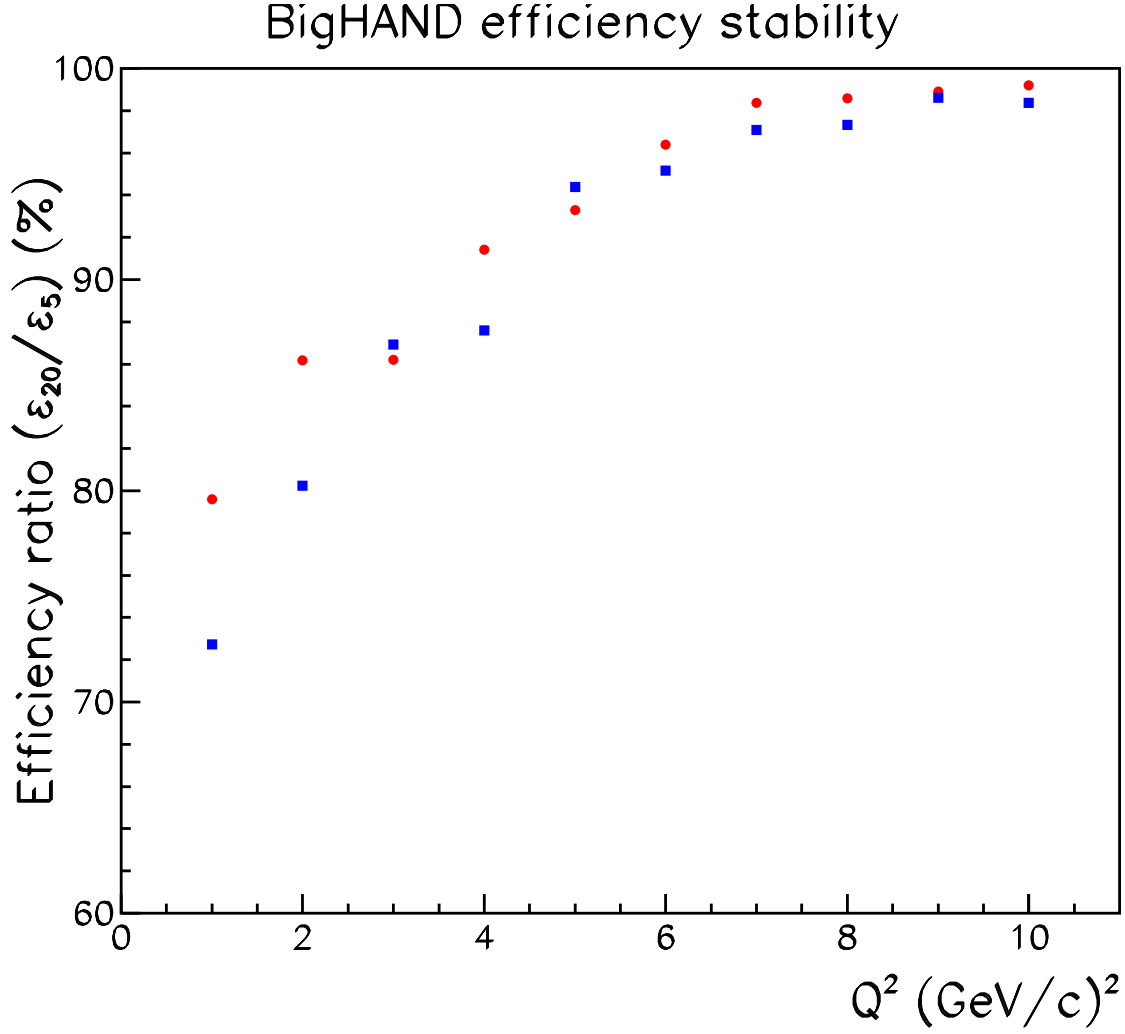
Figure 9: The predicted [44] *ratio* of the detection efficiency of BigHAND with a threshold of 20 MeV(ee) compared to a threshold of 5 MeV(ee) is shown for neutrons (blue squares) and protons (red circles) as a function of the central nucleon momentum associated with each Q^2.

Table 5: Fraction of detected quasi-elastic nucleons which fall inside the region calibrated (at the same kinematic point) with a) a single BigBite position for calibration or b) two off-set calibration positions.

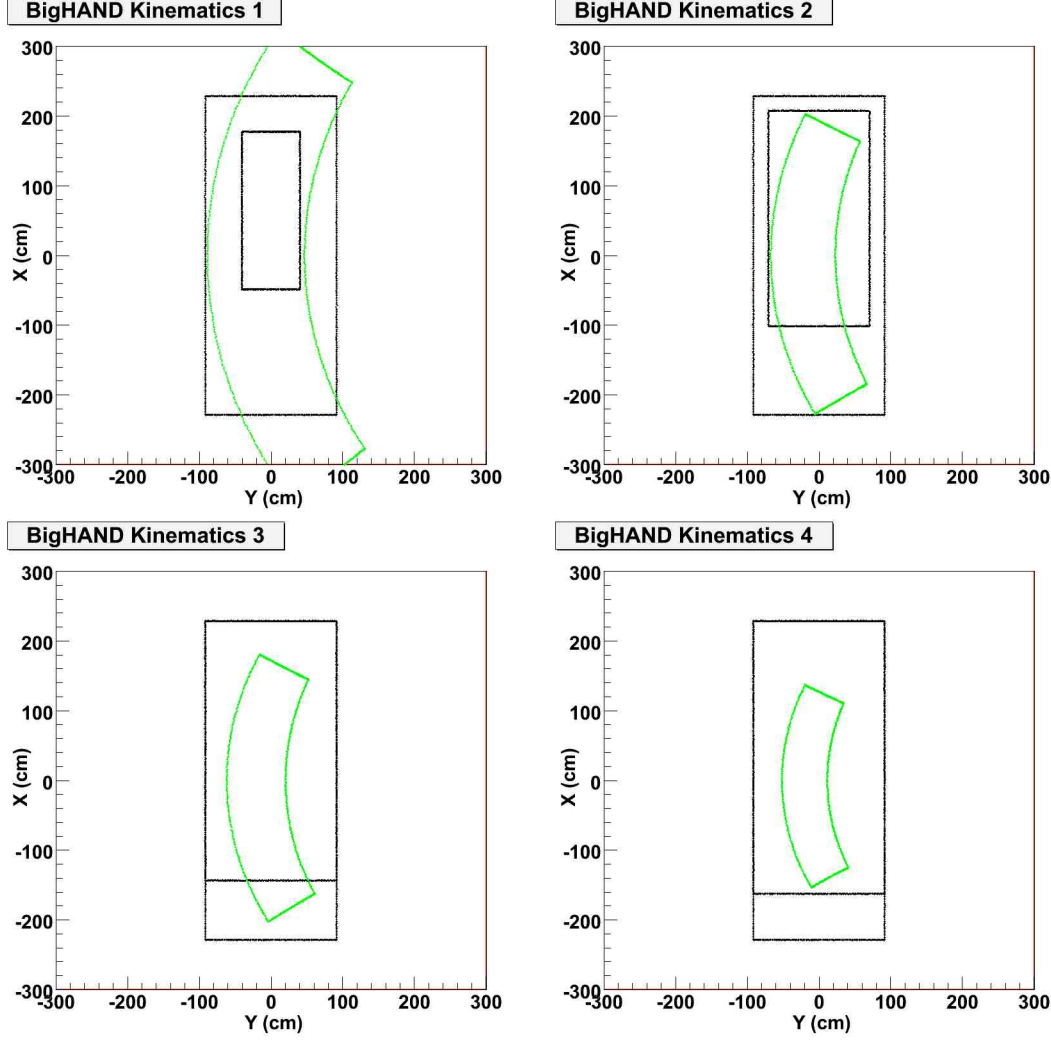| Q^2 (GeV/c)^2	a) Fraction (%) in Single Cal. Zone	b) Fraction (%) in Double Cal. Zone
3.5	93.3	100.
4.5	71.1	95.3
6.0	68.4	94.4
8.0	71.7	88.6

Figure 10: The face of the BigHAND detector is shown (rectangle) with a superimposed outline of the region covered by elastically scattered (calibration) nucleons for which the corresponding electron falls within the acceptance of BigBite when BigBite is positioned at the nominal scattering angle. Note that positive-x is downward, so the images are inverted. The four plots correspond to the kinematic points at which calibration measurements will be made: Upper left, $Q^2 = 3.5$, upper right, $Q^2 = 4.5$, lower left, $Q^2 = 6.0$, lower right, $Q^2 = 8.0$ $(\mathrm{GeV/c})^2$
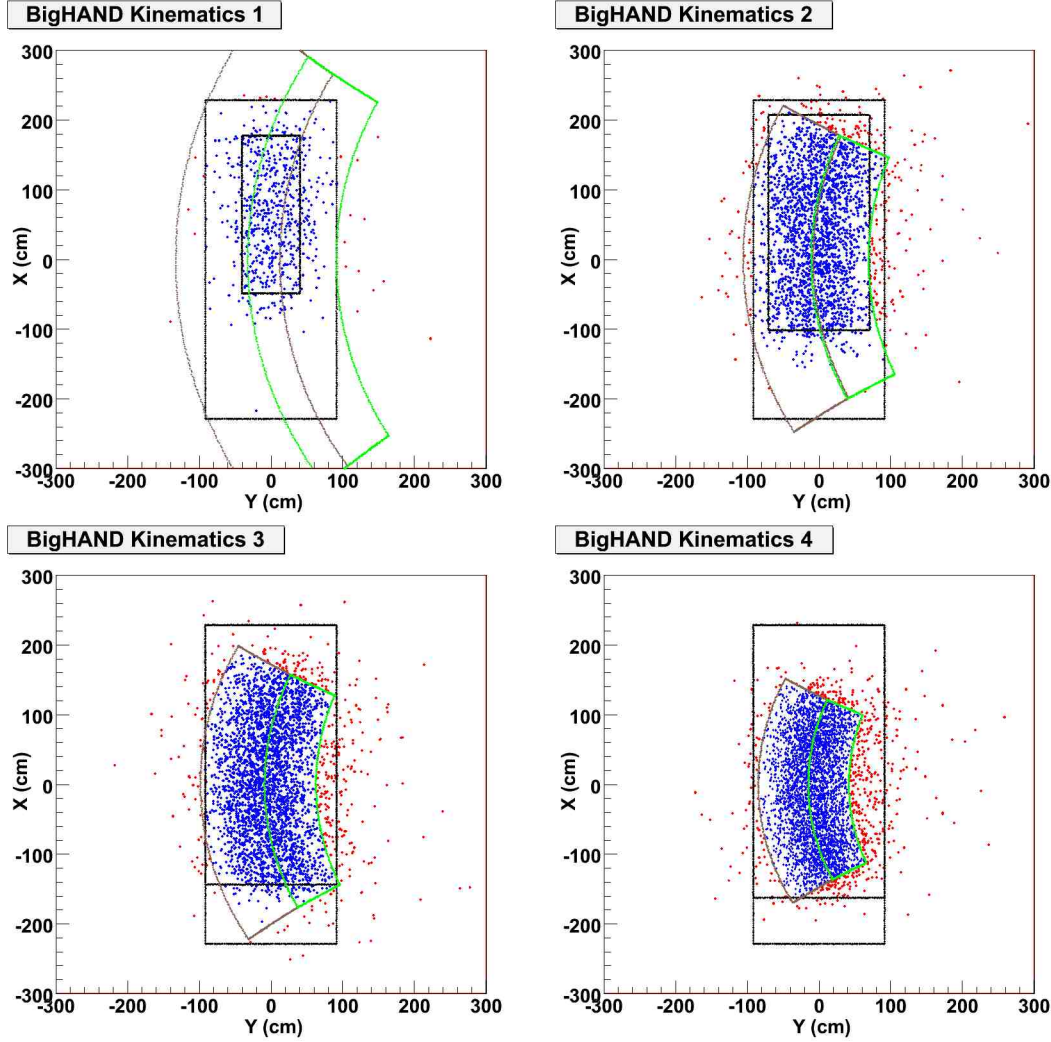
Figure 11: The face of the BigHAND detector is shown (large black rectangle) with a superimposed outlines of the regions covered by elastically scattered (calibration) nucleons for which the corresponding electron falls within the acceptance of BigBite when BigBite is positioned at the two planned calibration angles (shown as blue and green regions). Simulated quasi-elastic neutrons are shown, subject to the fiducial cut on electron acceptance which requires that $\vec{q}$ points towards the smaller black rectangle. Blue points indicate the neutron falls within the region calibrated at these kinematics. Red points fall outside the calibration region (and in some cases, outside the detector acceptance). Note that positive-x is downward, so the images are inverted. The four plots correspond to the kinematic points at which calibration measurements will be made: Upper left, $Q^2 = 3.5$, upper right, $Q^2 = 4.5$, lower left, $Q^2 = 6.0$, lower right, $Q^2 = 8.0$ $(\text{GeV/c})^2$

case Monte Carlo simulation, tuned using the lower energy measurements, will be used to extrapolate the efficiency calibration to the momentum of interest. Essentially, the observed efficiency at lower momentum can be used to determine an effective number of interaction lengths in sub-regions of the detector. These effective thickness can then be scaled to higher momentum by taking into account the known variation of hadronic cross-sections with momentum and a new efficiency can be predicted. This is a modest extrapolation since the hadronic cross sections change slowly as the nucleon momentum changes over the range from 2.6 to 5.1 GeV/c (see Fig. 12, note that zero is suppressed on the vertical scale). This results in the slow variation in BigHAND's efficiency seen in Fig. 5. The efficiency variation is seen to be quite modest over the entire range of interest $(3.5 \leq Q^2 \leq 8.0 \ (\text{GeV/c})^2)$ and to be almost constant at the highest Q^2. Table 5 shows that $\approx 95\%$ or more of the quasielastic events are expected to fall within the calibrated region except at the $Q^2 = 8.0 \ (\text{GeV/c})^2$ point for which 11.4% of events will require the use of an extrapolated calibration. Since Fig. 5 shows the efficiency to be changing very slowly in this kinematic range (Fig. 12 shows the nucleon cross-section to be essentially flat for the corresponding momentum $(p_N = 5.1 \ \text{GeV/c}))$, this extrapolation is expected to have small uncertainty. The same technique will be used to interpolate efficiencies for the two kinematic points for which calibration data will not be taken. The effective thickness will be determined for both the higher and lower calibration points, and will be interpolated. Despite the large size of BigHAND, a portion (one tenth) of its structure could be brought to the tagged neutron beam at Dubna for calibration. This could provide a cross check of the Monte Carlo simulation of momentum-dependence of efficiency.

6.2 Proton Calibration

Calibration of the detection efficiency for protons can be done straightforwardly, using a hydrogen target in place of the deuterium target and using BigBite to select elastic-scattering events. The recoil elastic protons have the same momentum as the protons at the center of the quasi-elastic peak, and so are ideal for calibrating the efficiency. This kinematic match is shown in Fig. 13 and 14 where BigHAND is divided into strips of polar angle and the momentum spectrum of quasi-elastic nucleons in each strip is overlaid with the spectrum of calibration nucleons.

Clean selection of tagged protons requires that BigBite be able to distinguish elastic events with negligible contamination from inelastic events, for which the 'tagged' nucleon might be absent or at a significantly different angle than predicted. Figure 15 shows the kinematic locus for elastic scattering kinematics (in the region of each of the kinematic points of interest) and the locus of the scattered-electron kinematics for pion-production threshold. The two are seen to be cleanly separated in both angle and energy. The bars superimposed on the plots indicate the anticipated resolution of BigBite in angle and energy.

As discussed above, the coverage of the calibration will be extended across a wider region of BigHAND by taking calibration data in two BigBite positions, as represented in Fig. 11.

6.3 Neutron Calibration

A clean *in situ* source of tagged neutrons at essentially elastic-scattering kinematics can be generated using a radiator to produce real photons which, in turn, produce neutrons through the p(γ, π^+)n reaction on a Hydrogen target. The calibration for each kinematic setting will be done at the same two BigBite settings discussed above for proton efficiency calibration. Since the kinematics of the
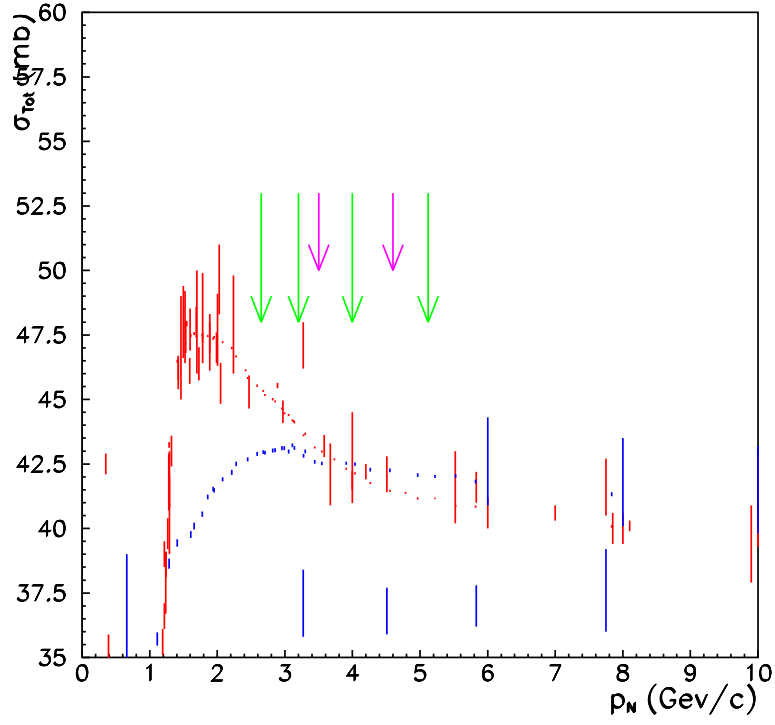
Figure 12: Total cross section [48] for proton-proton (red) and proton-neutron(blue). Some points with large errors have been suppressed. Green arrows indicate the central nucleon momenta for the four kinematic points at which calibration data will be taken. Magenta arrows indicate kinematic points for which interpolated calibrations will be used.
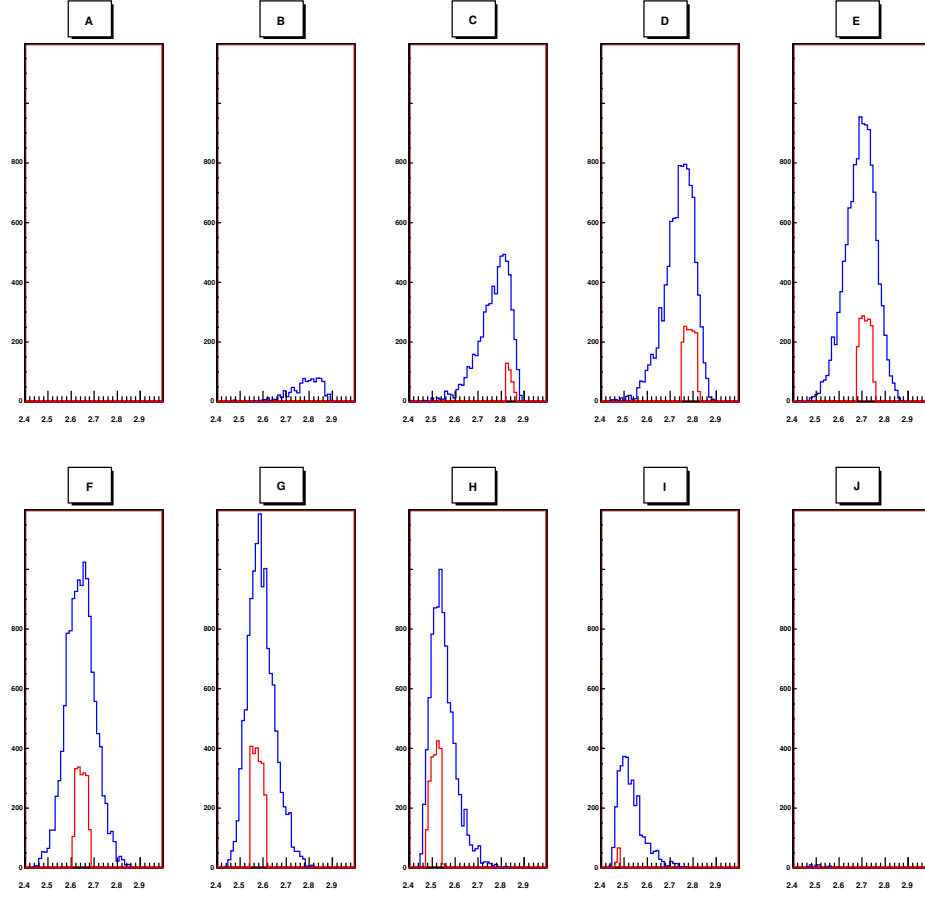
27

Figure 13: For the lowest Q^2 kinematic point, the kinematic overlap of the (elastic-kinematics) calibration nucleons with the quasi-elastic nucleons of interest is shown. The BigHAND acceptance is divided into ten strips in polar angle. Each plot represents the nucleon momentum spectrum falling on a strip (blue) and the momentum spectrum of calibration nucleons reaching that strip (red). Note that zero is suppressed on the horizontal scale. Horizontal scale on each plot is 2.4 to 3.0 GeV/c. The width of the quasi-elastic nucleon momentum distribution is seen to be modest and reasonably centered on the calibration data.
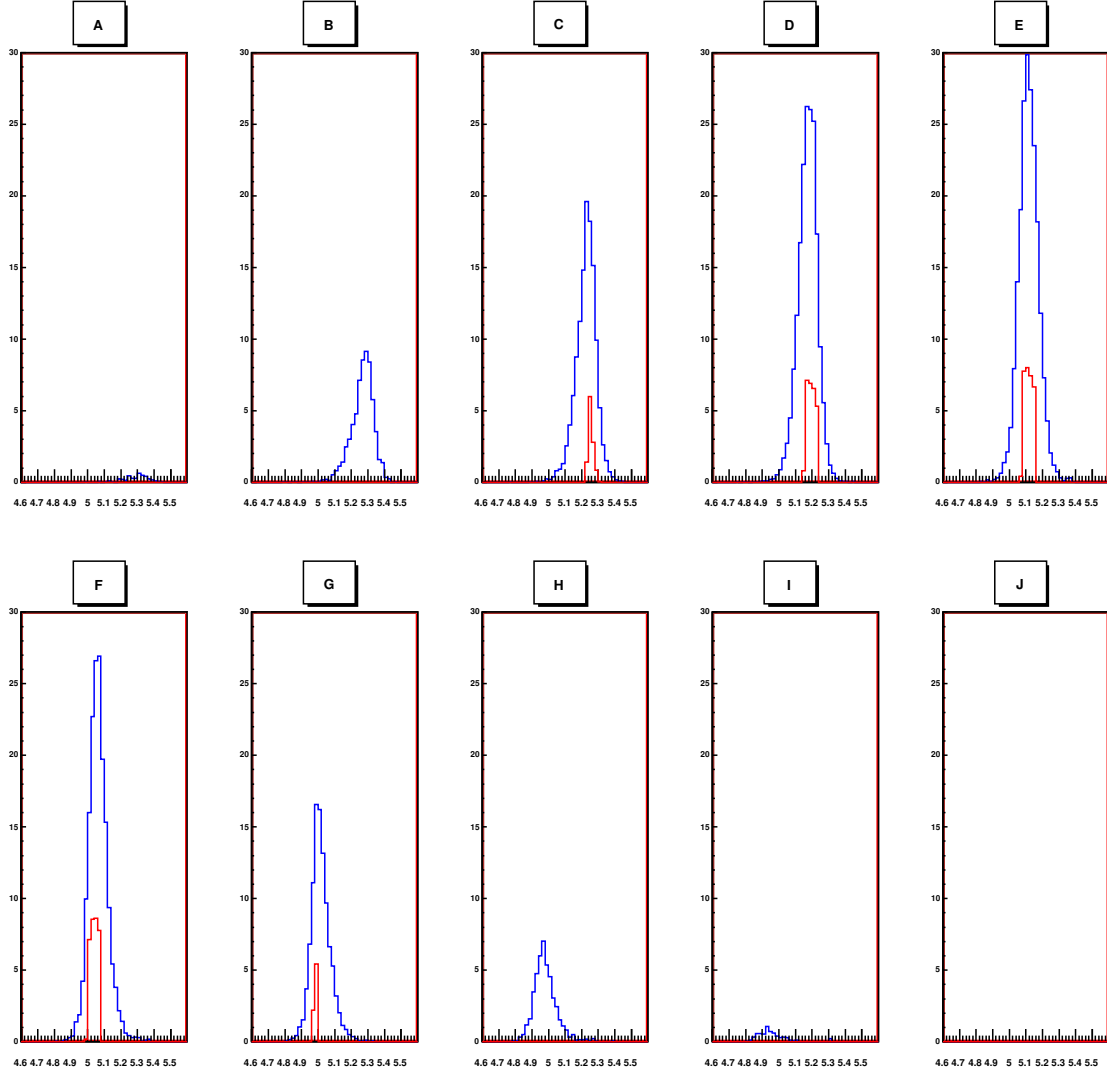
Figure 14: Same as 13, but for the highest Q^2 kinematic point. Horizontal scale on each plot is 4.6 to 5.6 GeV/c.
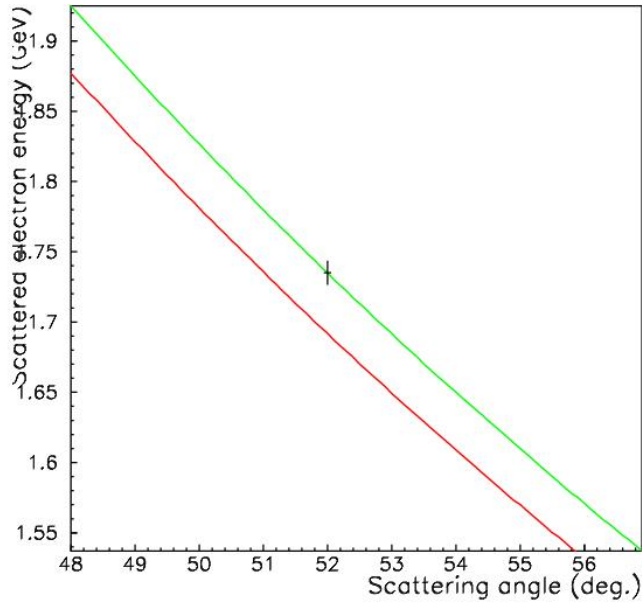
Figure 15: Scattered electron energy versus angle for elastic scattering from the nucleon (green)

and for pion-production threshold (red). The bars indicate the BigBite resolution in momentum and angle. The plot shows the clean kinematic separation at the $Q^2 = 8$ $(\text{GeV/c})^2$ kinematic point. The separation is cleaner at all other kinematics.

Table 6: Kinematics limiting the part of bremsstrahlung spectrum which can be used for neutron efficiency calibration.

Q^2 (GeV/c)^2	E_{beam} (GeV)	θ_e	E_π^{max} (γ,π) (GeV)	E_π^{max} $(\gamma,2\pi)$ (GeV)	E_π^{limit} (γ,π) (GeV)	E_γ^{min} (GeV)	$\int \Gamma\, dk$
3.5	4	37.5°	2.12	2.043	2.074	3.83	0.0029
4.5	4	49.5°	1.603	1.540	1.563	3.78	0.0039
6	5	48.1°	1.805	1.747	1.773	4.80	0.0028
8	6	52.°	1.73	1.688	1.713	5.79	0.0025

For each kinematic point, the values given are: $E_\pi^{max}(\gamma,\pi)$, the end-point energy for π production; $E_\pi^{max}(\gamma,2\pi)$, the π end-point energy for 2π production; $E_\pi^{limit}(\gamma,\pi)$, the minimum π energy to be used for calibration (to exclude $E_\pi^{max}(\gamma,2\pi)$ by 1.5%); E_γ^{min}, minimum photon energy giving $E_\pi(\gamma,\pi)$ above $E_\pi^{limit}(\gamma,\pi)$; $\int \Gamma\, dk$, the photon flux (per electron) integrated [45] from E_γ^{min} to the photon end point (assuming 6% Cu radiator).

reaction are essentially those of elastic scattering, the overlap of the calibration neutron spectrum with the quasielastic spectrum is the same as that shown in Fig. 13 and 14.

The end-point method can be used to select the reaction of interest and exclude multi-body final states. In particular, for each beam energy, the maximum possible π^+ momentum for three-body $p(\gamma,\pi^+)\pi N$ reaction sets the scale of the lowest π^+ momentum which can safely be used to select the desired two-body channel. Clear identification of the exclusive $p(\gamma,\pi^+)n$ reaction will be ensured by requiring that the π^+ momentum be at least 1.5% above the kinematic limit for the three-body channel. With 0.5% momentum resolution in BigBite, the 1.5% gap between the lowest π^+ momentum used and the highest momentum from 2π-production provides an adequate safety margin. Production of 2π background at this kinematic limit will be negligible both because it requires photons at the bremsstrahlung end point and because the phase-space vanishes. This minimum acceptable π^+ momentum, in turn sets the limit for the minimum usable photon energy and the part of the bremsstrahlung end point region which will actually be used for calibration events. Table 6 shows the region of the photon end point which can be used for neutron calibration at each kinematic setting. For the lowest Q^2 point, for example, the three-body reaction cannot produce pions above 2.043 GeV. For safety, pions will be identified as coming from the two-body calibration reaction only if they lie between 2.075 GeV and the kinematic limit of 2.12 GeV.

The real photons used for the $p(\gamma,\pi^+)n$ calibration reaction will be generated using a copper 6% radiator upstream of the LH$_2$ target. Maintaining the same limit on rate in BigBite then requires that the beam current be reduced by a factor of four for these measurements. While real photons interacting with well-defined 2-body kinematics will dominate, roughly one quarter of the rate is expected to originate from virtual-photon interactions. The virtual-photon contribution can be studied (along with the corresponding distribution of neutrons in BigHAND) by running without a radiator and measuring neutrons associated with the $p(e,\pi^+)$ reaction. Because this is a relatively small correction, allocation of beam time would be optimized to yield the minimal error on the real-photon calibration by spending only a fraction as much beam time on running without a radiator. (Taking the virtual and real cross sections to be equal and the neutron acceptance and efficiencies

to be as large for virtual production implies that the error bar would be minimized by dedicating 20% of the neutron-calibration time to running without a radiator.)

7 Simulations

At high Q^2 the kinematic separation of quasi-elastic and inelastic events becomes more washed-out by the kinematic-broadening effects of Fermi motion in the deuteron. Also the size of the inelastic cross section relative to the quasi-elastic grows rapidly with increasing Q^2. A simulation is needed to determine whether there is a serious problem with contamination of the quasi-elastic coincidence signal by inelastic events for which a nucleon accidentally hits the BigHAND near where a quasi-elastic nucleon would be expected.

This section will present the technical details of the implementation of the simulations, including the normalization of the inelastic spectrum relative to the quasi-elastic. The next section will present the results of the simulations.

7.1 Quasi-elastic

Simulation of the quasi-elastic signal was carried out in a spectator model in which the virtual photon was assumed to interact with only one nucleon while the other simply escaped. This implies that the spectator nucleon is projected into 'on-shell' kinematics by the interaction (with whatever initial momentum it has) and so the initial off-shell mass of the struck nucleon is determined by the requirements of energy conservation. While off-shell effects where included at the kinematic level, no attempt was made to modify the electron-nucleon scattering cross section to reflect the off-shell nature of the struck nucleon. For these simple signal-to-noise estimates, the scaled dipole form factors were assumed for the nucleons (except the Galster parameterization was used for the neutron electric form factor). As described below, kinematic effects of the initial motion of the nucleon were reflected by calculating the cross section based on the electron energy and scattering angle as determined in the rest frame of the scattered nucleon.

The momentum distribution of nucleons was taken from the momentum-space wave-function (non-relativistic Fourier transform of spatial wave-function) for a Lomon and Feshbach deuteron potential. The particular model used (#10 from reference [46]) gave 5.79% D-state and included a hard core. The hard core is reflected in a high-momentum tail in the momentum-space wave-function making this a somewhat 'worst case' simulation.

In brief, the steps of each quasi-elastic event simulation are summarized here. A Fermi momentum was chosen for the struck nucleon based on the probability distribution for magnitude of p derived from the deuteron wave-function. A direction was chosen isotropically. The corresponding kinetic energy of the the on-shell spectator was subtracted from the deuteron mass to find the kinematically-consistent initial energy of the struck nucleon from which the (off-shell) invariant mass of the struck nucleon was found. The beam electron was then rotated and boosted to a frame in which the nucleon was at rest (and the electron was rotated back onto the z-axis). A scattering angle was then chosen isotropically (flat in ϕ and in $\cos\theta$) and the elastic scattering cross section was evaluated for these rest-frame initial kinematics. The scattered energy was calculated with the added requirement that the off-shell initial-state nucleon be promoted to an on-shell nucleon in the final state. Some 'sanity cuts' were applied to eliminate extreme cases in which the quasi-elastic

model was clearly pushed beyond the range of applicability, such as cases with off-shell invariant mass of the struck nucleon being less than 10% of the nucleon mass or final electron energy being unphysical. All boosts and rotations were then inverted on the final-state particles to return them to the lab frame. No kinematic weighting was done on the distributions of Fermi momentum or scattering angle to reflect the greater probability of scattering at small angles and at kinematics which lead to lower electron energy in the nucleon rest frame. The higher weighting of these events was reflected in the calculated cross section, which was then used to weight the entries made to the final-state distributions. Thus the simulation not only properly accounted for these kinematic effects, it also resulted in properly normalized cross sections for the simulated reaction. To select the quasi-elastic events of interest, an acceptance cut was imposed to require that the electron fell into the BigBite acceptance while the scattered nucleon fell into the BigHAND acceptance. The effects of finite-resolution were then incorporated by smearing the final electron-energy angle and energy by Gaussian distributions to simulate the BigBite resolution and similarly smearing the detected nucleon angle to reflect the BigHAND resolution. The resulting quantities were then used to calculate W^2 and θ_{pq} and the simulated distributions of the quantities of interest were incremented, weighted by cross section. Here θ_{pq} is the angle between the calculated $\vec{q}$ direction and the observed scattered nucleon direction while W^2 is the squared missing-mass of the hadronic system as calculated assuming a stationary proton target (i.e. $W^2 = (m_p + \omega)^2 - (\vec{q})^2 = m_p^2 + 2m_p\omega - Q^2$).

7.2   Inelastic

The term "inelastic" is used here to imply particle production and is exclusive of quasi-elastic events. Simulation of inelastic events required a more sophisticated model for the basic interaction on the nucleon. This was done with the use of the Genev physics Monte-Carlo [49] written by the Genoa group and used extensively in simulations for CLAS. This program is designed to simulate with, reasonable empirical distributions, production of multi-pion final states and production and decay of Delta's, rho mesons, and omega meson (phi meson production was not enabled when the simulations were run). It can simulate neutron or proton targets and both were used in simulating inelastic events from the deuteron.

The smearing effects of Fermi motion for quasi-free inelastic production from the nucleons in the deuteron were included in a similar way to that described above for the quasi-elastic production. There was, however, no mechanism to put the initial-state nucleon off-shell for the initial state used by Genev. The spectator model was therefore implemented by treating the initial state as two on-shell nucleons with equal and opposite Fermi-momentum (in the deuteron rest frame). The effective violation of conservation of energy implied by this approximation is modest (a few tens of MeV) and is expected to have the effect of widening tails and so causing backgrounds to be over-estimated if anything.

Final-state distributions were simulated separately for electro-production off the neutron and proton. The same momentum-state wave-function was used to generate the initial momentum distribution of the target nucleons. After rotating and boosting to the nucleon rest frame the energy of the incident electron was passed to a Genev-based subroutine which simulated a single inelastic event for the chosen effective beam energy. The scattered electron direction was selected randomly (both θ and azimuthal angle, ϕ) by Genev based on cross-section-weighting subject to constraints on W^2 and Q^2, discussed below. The predicted final-state particles were then boosted and rotated back to the lab frame by reversing all boosts and rotations done to the initial-state

particles. In order to make effective use of simulated events without biasing distributions, those events which had a final electron azimuthal angle outside the range of $-30°$ to $+30°$ were rotated about the beam direction by an angle chosen to give a final azimuthal angle chosen randomly within that range. This enhanced the yield of events within the BigBite acceptance but didn't affect distributions which had, at minimum, a requirement of a hit in BigBite.

The range of Q^2 and W^2 to be generated by Genev was selected empirically since the effects of Fermi motion made it difficult to predict the significant range *a priori*. A low-statistics run of the simulation with a broad range was subjected to the acceptance cut of BigBite for the angle(s) of interest for the beam energy being simulated. The resulting Q^2 and W^2 distribution showed clear peaks in the regions which were relevant for scattering into BigBite. High statistics runs were then done with those ranges selected for generation of Genev events.

Full kinematic information was written out for each event (including particle identification for each four-vector). These were then selected to produce samples of interest for each kinematic point which would have an electron within the BigBite acceptance. The effects of finite detector resolution were folded in (by smearing of each four-vector) before calculation of kinematic quantities of interest such as W^2 and θ_{pq}.

7.3   Inelastic Background Normalization

A fundamental difference between the quasi-elastic and inelastic simulations is that the inelastic simulation produced simulated events without a corresponding cross section by which to weight them. While the relative cross sections were accounted for in the probability of generation of different types and topologies of events, an overall normalization is needed to allow comparison of the inelastic events (from each target nucleon) with the quasi-elastic results.

Normalization of inelastic to quasi-elastic cross sections was done empirically, using SLAC spectra for single-arm electron scattering from the deuteron. Figure 16 shows spectra from [50] and [26] used for the normalization. The kinematic coverage of those measurements (truncated to the W^2 range of relevance) is shown in Fig. 17 with the same colors as in Fig. 16 to distinguish the two data sets. Two conveniently chosen ranges were used to characterize the cross sections in the quasi-elastic and inelastic regions. These are indicated in Fig. 16 as green bars indicating the limits selected for the "Quasi-elastic region" ($0.5 < W^2 < 0.88$ GeV^2) and red bars indicating the limits selected to define the "Inelastic region" ($1.3 < W^2 < 1.7$ GeV^2). As can be seen from the figures, the regions were chosen to give samples which were almost purely representative of the indicated final state, without significant contamination of inelastic events in the Quasi-elastic region or *vice versa*. The Inelastic region was also chosen close to the quasi-elastic peak so it would be representative of the events which would be likely to cause background.

Within the quasi-elastic model, the kinematic variation of cross-section within the Quasi-elastic region would be expected to follow the sum of the elastic cross sections for scattering from the proton and neutron. The numerically summed cross section in the Quasi-elastic region of each spectrum was divided by the predicted sum of proton-elastic and neutron-elastic (based on scaled-dipole and Galster) to obtain a measured strength (which was quite stable at a value of ≈ 0.35). Similarly, based on

$$\frac{d^2\sigma}{d\Omega dE'} = \frac{\alpha E'(W^2 - m_p^2)/(2m_p)}{4\pi^2 Q^2 E} \frac{2}{1-\epsilon}(\sigma_T(W^2, Q^2) + \epsilon\sigma_L(W^2, Q^2))$$

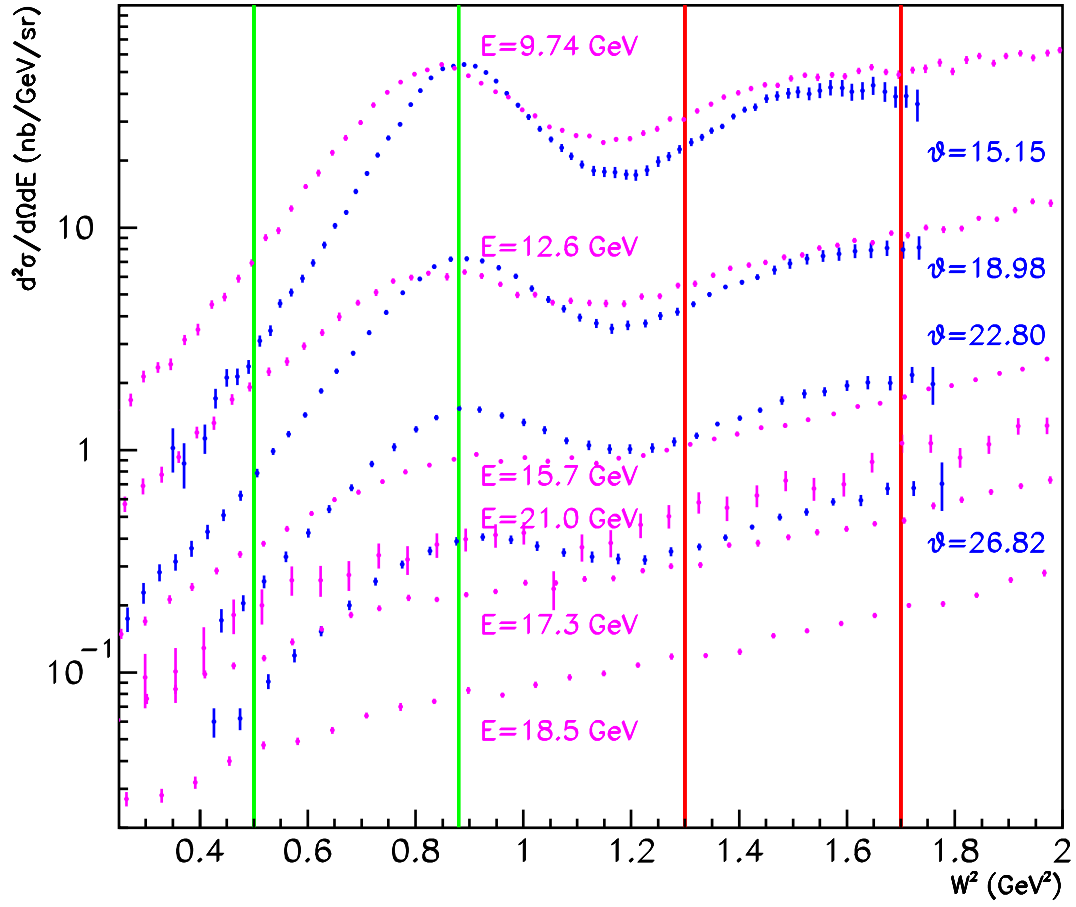the kinematic factors were divided out of each bin of the double-differential cross section in the In-

Figure 16: Measured single-arm spectra from SLAC covering the quasi-elastic and inelastic regions. Blue points were taken at E=5.507 GeV and indicated angle (in degrees). Magenta points were taken at indicated energy and $\theta = 10°$.
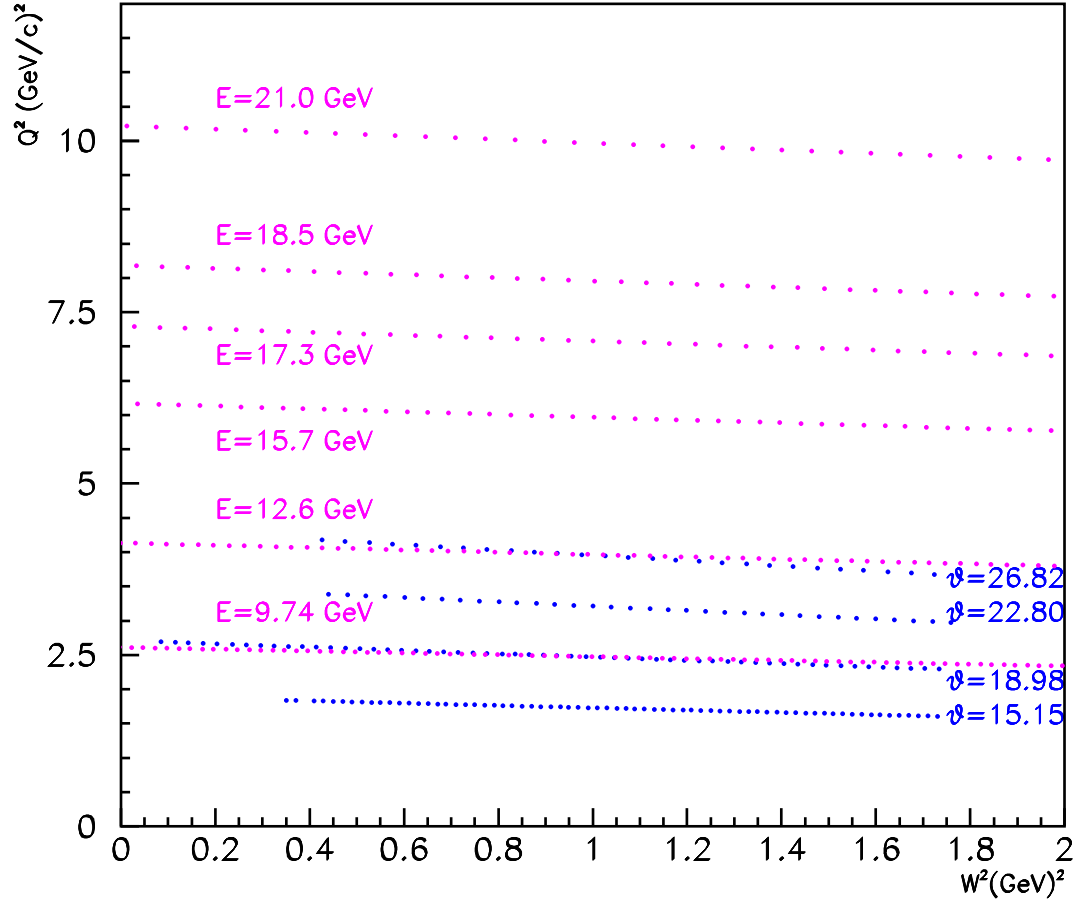
Figure 17: The Q^2 vs. W^2 coverage corresponding to the spectra of the previous figure.

elastic region to yield the corresponding value of $(\sigma_T + \epsilon \sigma_L)$. Since the non-resonant background dominates over Δ production in these spectra, a non-resonant empirical scaling of $\sigma_L/\sigma_T \approx 0.25/\sqrt{Q^2}$ was used to allow σ_T (summed over the Inelastic region) to be extracted for each spectrum. (An alternate extreme would be to treat the inelastic cross section as purely transverse, as it might be if the Δ dominated. This was tried and resulted in only a modest change in the predicted inelastic strength at the the kinematics of interest.) The inelastic/quasi elastic strength can then be characterized as the ratio of the extracted σ_T from the Inelastic region divided by the scaled cross-section from the Quasi-elastic region. This ratio (for both sets of SLAC kinematics) was found to be reasonably well parameterized as a simple parabolic function of Q^2 ($r = 0.015\frac{Q^2}{(\text{GeV/c})^2}$). This form was then used to predict the inelastic cross section within the Inelastic region for the Q^2 applicable for the beam energy and scattering angle of the kinematics of interest. These were found as multiples of the summed simulated cross section in the Quasi-elastic region (divided by the sum of proton and neutron elastic cross sections).

This gave the total normalization of the inelastic cross section. It remained to find individual scaling factors for the proton-target and neutron-target inelastic cross section to simulate the deuteron cross section. The inelastic cross section on the neutron was taken to be half of the inelastic cross section on the proton. Since the final state distributions (including individual measure of proton-coincidences or neutron-coincidences) were almost identical for the two assumed targets, the final results are almost insensitive to this choice of relative strength. This then allowed scaling factors to be determined to scale number of simulated events to double-differential cross section. These normalized results are shown in the next section.

Figure 18 compares one example predicted deuterium spectrum to our actual spectra [40, 41] on Hydrogen and ^{3}He at similar kinematics taken with BigBite. The beam energy and scattering angle of the measurements are different (see caption) but they are at very similar Q^2 to the lowest proposed kinematic point. Quantitative comparisons are not possible, but the Hydrogen peak is seen to be much narrower than the predicted deuterium peak (as expected) while the ^{3}He quasi-elastic peak is so wide it is not resolved from the inelastic background. The height of the inelastic background (relative to the height of the quasi-elastic peak) can be seen to be qualitatively similar indicating, at least, that the background is not grossly underestimated in the simulation.

Similarly, Fig. 19 shows an example predicted deuterium spectrum, with a proton coincidence in BigHAND. This is compared to our actual spectra [40, 41] on Hydrogen and ^{3}He at similar kinematics taken with BigBite and with a coincidence (neutron or proton) demanded in BigHAND. The Hydrogen spectrum is now seen to be much narrower than the deuterium quasi-elastic peak, confirming that instrumental resolution is a small effect compared to Fermi smearing. The inelastic background at $W^2 \approx 2$ GeV^2 in ^{3}He is seen to be similar to the height of the quasi-elastic peak. Quantitative evaluation of the inelastic-to-quasielastic ratio of the simulation is not possible since the conditions are not identical. The narrower deuterium peak would be expected stand out more than the more Fermi-smeared ^{3}He peak. Also, random-time coincidence have not been subtracted from the ^{3}He data and, as can be seen from Fig. 18, are expected to preferentially fall in the inelastic region. The estimated background (relative to quasi-elastic) in the simulation is seen to be comparable to that observed.

A test of the Monte-Carlo at the highest kinematic point ($Q^2 = 8$ (GeV/c)^2) is shown in Fig. 20. SLAC data [26] taken at a similar Q^2, but different beam energy and angle is compared to the Monte-Carlo prediction for single-arm electron scattering from deuterium. The SLAC data was

taken at E=18.5 GeV and $\theta = 10°$. It is compared to the Monte-Carlo prediction at the same momentum-transfer at E=6.0 GeV and $\theta = 52.0°$. **There are no adjustable parameters.** The Monte-Carlo spectrum has simply been scaled up by the ratio of prediction for the ratio of deuteron quasi-elastic cross sections. This cross section was predicted (at each set of kinematics) as the sum of the dipole-prediction cross-section on the proton plus that on the neutron. The agreement is seen to be excellent and the inelastic background is, if anything, overestimated.

8   Inelastic Background

Summary plots from the simulations of inelastic contributions are shown in Figures 21 through 24. Each figure represents one of the kinematics shown in Table 1. The simulation results are not shown for the for the $Q^2 = 5.25$ and 7 $(GeV/c)^2$ kinematic points. They are qualitatively similar to those shown.

In each figure the upper left plot gives the missing-mass spectrum integrated over the acceptance of the experiment. These are single-arm spectra such as would be obtained using BigBite alone. These figures are not of direct relevance to the coincidence experiment proposed here. They are intended only to set the scale of how difficult single-arm quasi-elastic measurements would be and to demonstrate that the simulated single-arm spectra are qualitatively similar to the measurements show in Fig. 16. In all simulated spectra, the statistical fluctuations reflect the statistics of the Monte-Carlo simulations and are not intended to simulate the statistics acquired by the proposed experiment.

The upper right plot in each figure shows the proton-coincident quasi-elastic and inelastic spectra and their sum. The lower left plots show the equivalent neutron-coincident spectra. The kinematic broadening and the large inelastic cross sections are seen to result in a large contribution of inelastic events under the quasi-elastic peak, particularly at high Q^2. Without additional cuts to reduce this contamination, this would present a significant problem for these measurements.

The lower right plots show, for the neutron-coincident data, the measured distribution of θ_{pq}. As mentioned above, θ_{pq} is the angle between direction of the nucleon's momentum $(\vec{p})$, reconstructed from the position of the hit on BigHAND, and the momentum-transfer vector $(\vec{q})$, as reconstructed based on the scattered-electron's energy and direction. For elastic scattering from a nucleon at rest, θ_{pq} would peak sharply at zero, having a finite width only due to measurement resolution. For quasi-elastic scattering, θ_{pq} is broadened by the unknown initial momentum of the struck nucleon. However, it is seen to still be sharply peaked. At the $Q^2 = 8$ $(GeV/c)^2$ point shown in Fig. 24, the quasi-elastic θ_{pq} distribution is seen to be almost entirely contained below $\theta_{pq} = 2°$. The distribution for inelastic events is seen to be much wider. This provides an additional cut which can be used to select the quasi-elastic events of interest and reject the background from inelastic events. Furthermore, the linear rise of the inelastic distribution (which is a geometric effect, reflecting a roughly constant density of nucleon hits per unit area in the region pointed to by the $\vec{q}$ vector) suggests the possibility of correcting for residual inelastic contamination by extrapolating the large-angle θ_{pq} spectrum into the region of the cut and predicting the contribution of inelastic events surviving the cut.

From the figures presented above, it is clear that the inelastic background is largest in the case of neutron-coincident measurements at the highest Q^2. For this case, Fig. 25 presents additional results from the simulation demonstrating the effect of cuts on θ_{pq}. The signal-to-noise ratio is

Figure 18: Predicted spectrum on Deuterium (Top) at $Q^2 = 3.5$ GeV^2 (E=4 GeV, $\theta = 37.5°$) is compared to measured spectra taken with BigBite on Hydrogen (Middle) and ^{3}He (Bottom) targets at $Q^2 = 3.4$ GeV^2 (E=3.29 GeV, $\theta = 51.6°$). All spectra are single-arm spectra with no coincidence requirement.
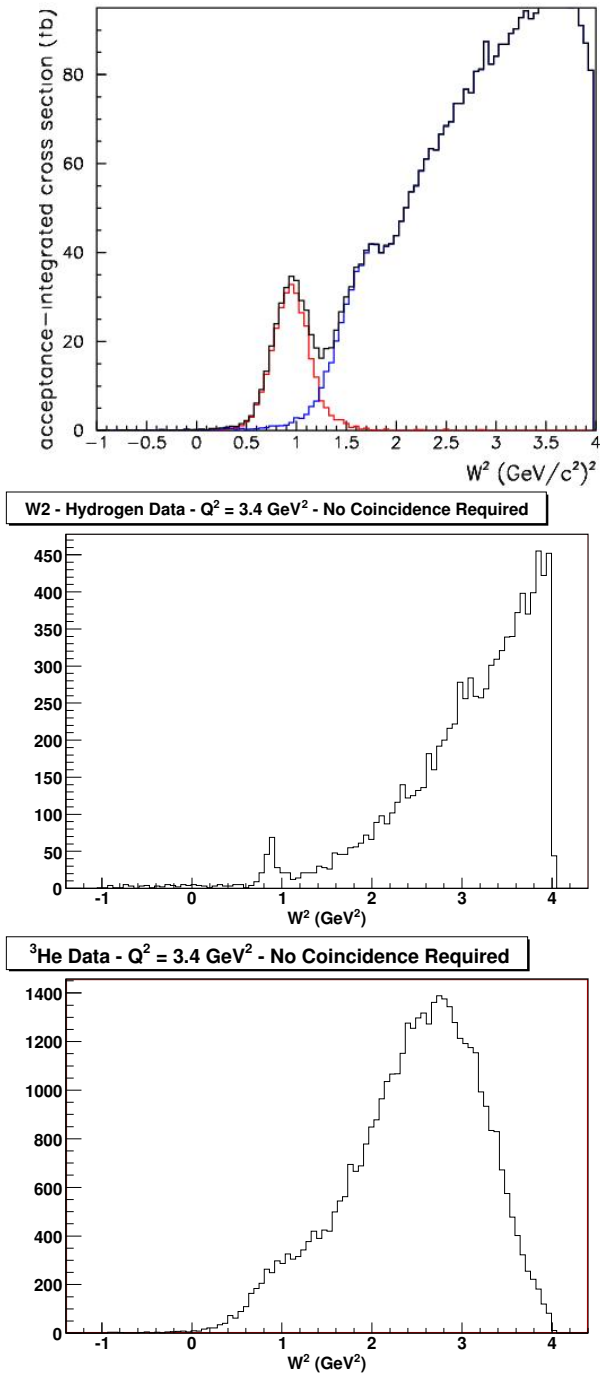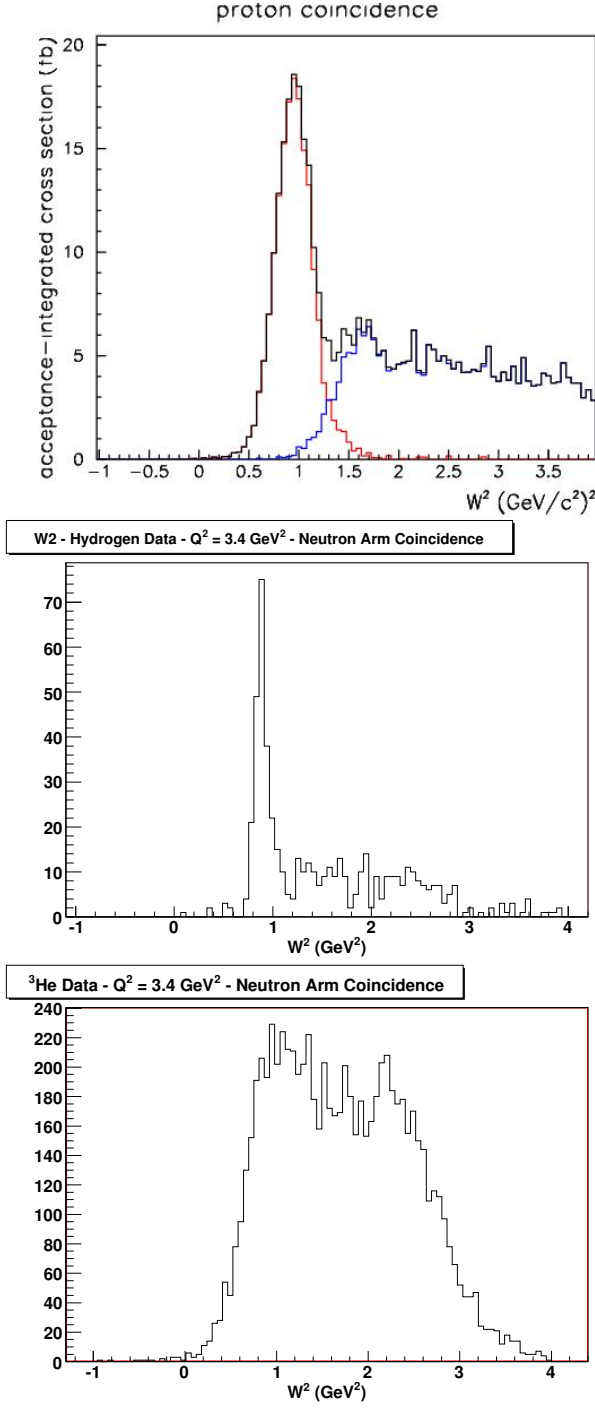
Figure 19: Predicted spectrum on Deuterium (Top) at $Q^2 = 3.5$ GeV^2 (E=4 GeV, $\theta = 37.5°$) is compared to measured spectra taken with BigBite on Hydrogen (Middle) and ^{3}He (Bottom) targets at $Q^2 = 3.4$ GeV^2 (E=3.29 GeV, $\theta = 51.6°$). The simulated spectrum demands a proton in coincidence anywhere in BigHAND. The real spectra demand a hit in BigHAND but do not distinguish between proton and neutron coincidences. Accidental coincidences have not been subtracted in the measured spectra.
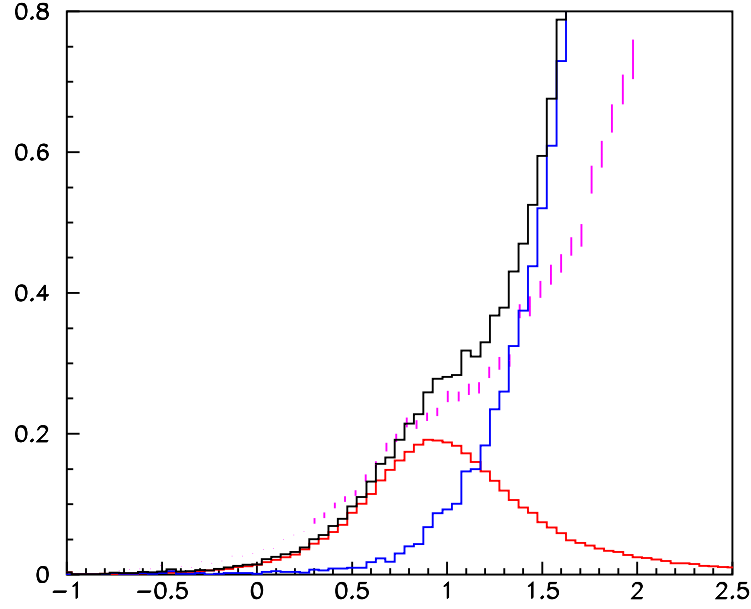
Figure 20: A measured spectrum [26] for single-arm electron scattering from deuterium (E=18.5 GeV, $\theta = 10°$) is compared to the Monte-Carlo prediction at the same momentum-transfer (the $Q^2 = 8$ point in the present proposal, at E=6.0 GeV, $\theta = 52.0°$). The data points are shown in magenta, the Monte-Carlo prediction in black. (The quasi-elastic contribution is shown in red, while the inelastic prediction is in blue.) **There are no adjustable parameters.** The Monte-Carlo spectrum has simply been scaled up by the ratio of (dipole-approximation) prediction for the ratio of deuteron quasi-elastic cross sections.

Figure 21: Summary of simulations of inelastic background (blue) and quasi-elastic (red) cross section for the $Q^2 = 3.5 \ (\mathrm{GeV/c})^2$ kinematic point.
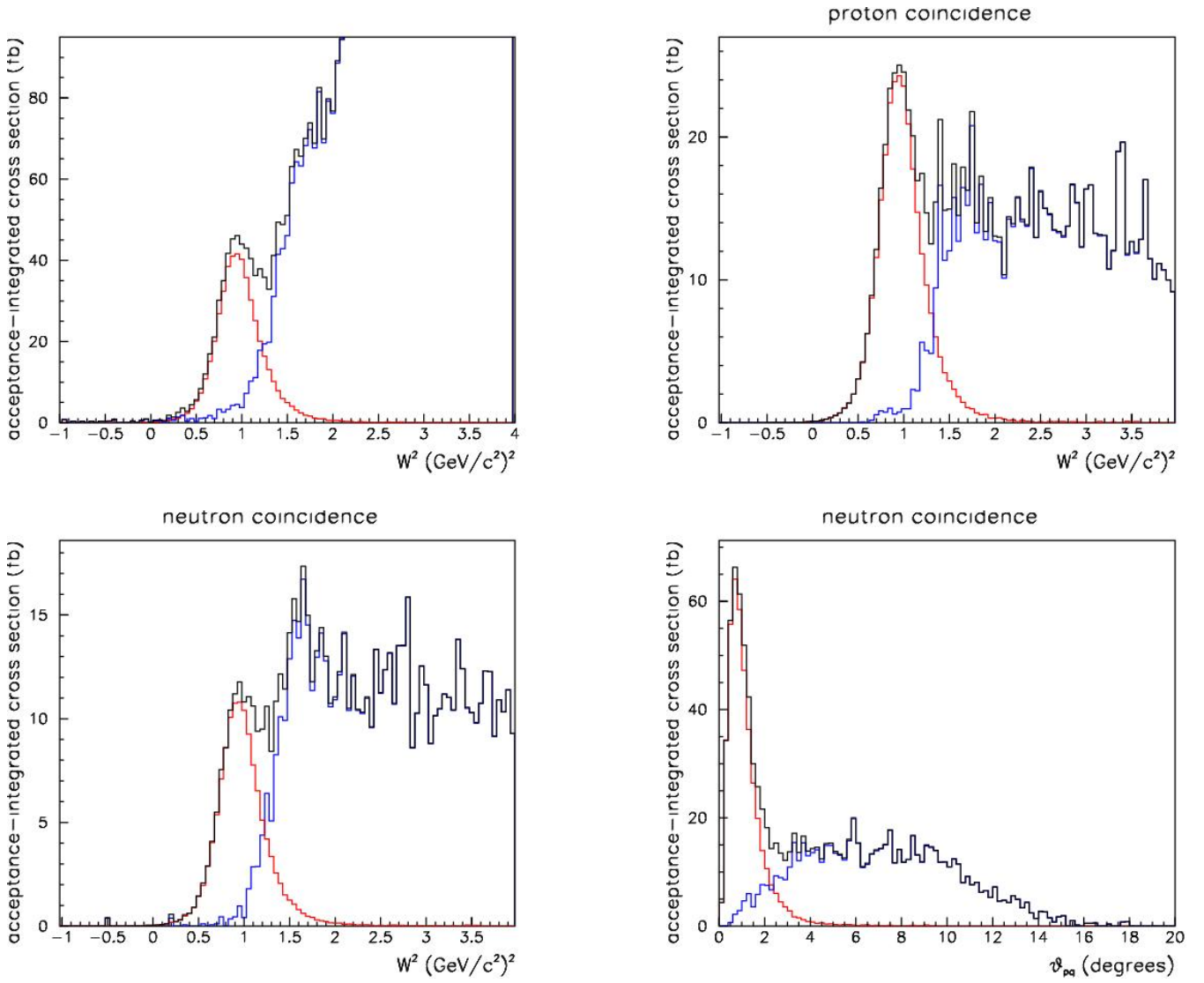
Figure 22: Summary of simulations of inelastic background (blue) and quasi-elastic (red) cross section for the $Q^2 = 4.5$ (GeV/c)^2 kinematic point.
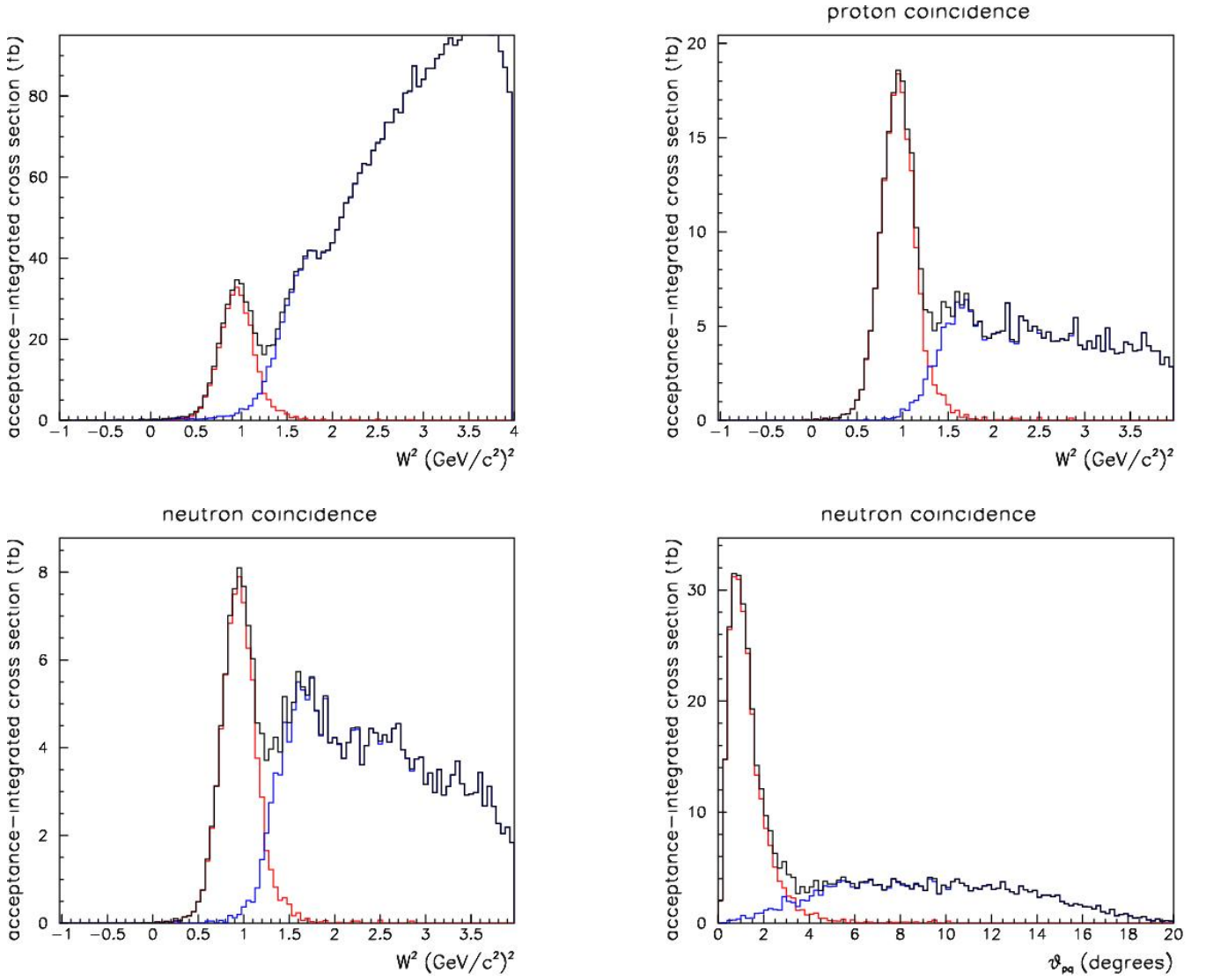
43
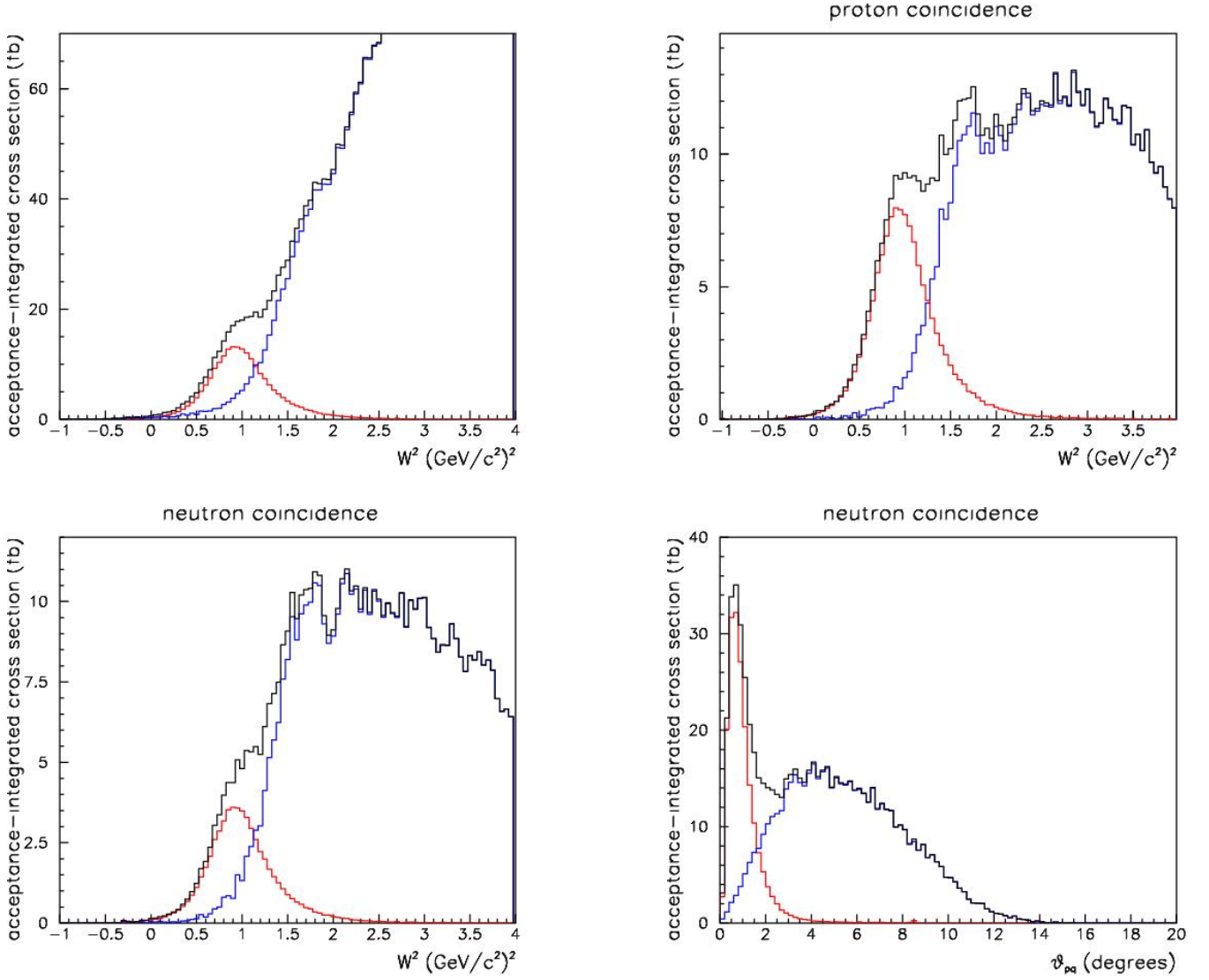
Figure 23: Summary of simulations of inelastic background (blue) and quasi-elastic (red) cross section for the $Q^2 = 6.0$ (GeV/c)^2 kinematic point.
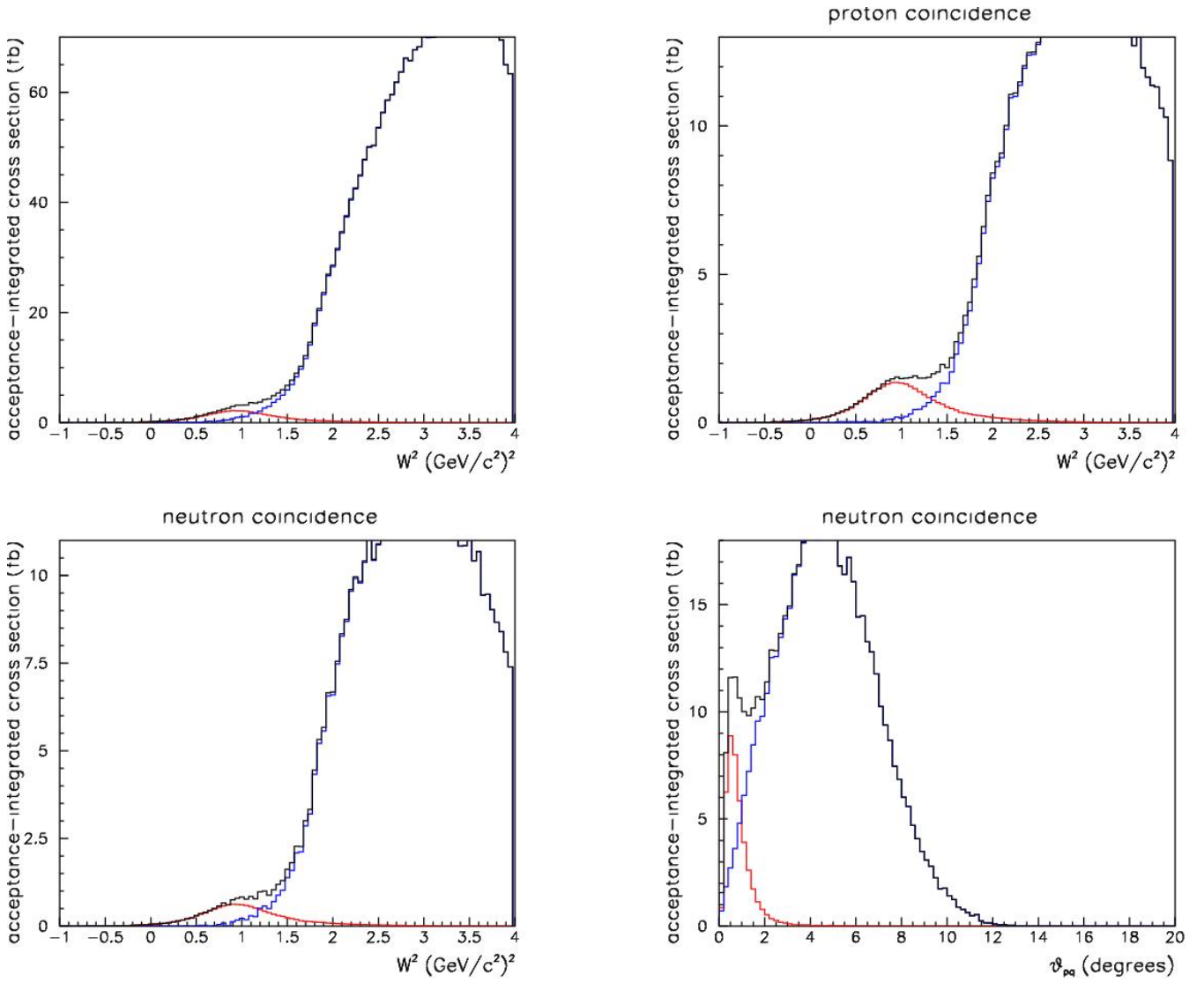
Figure 24: Summary of simulations of inelastic background (blue) and quasi-elastic (red)cross section for the $Q^2 = 8.0$ (GeV/c)^2 kinematic point.
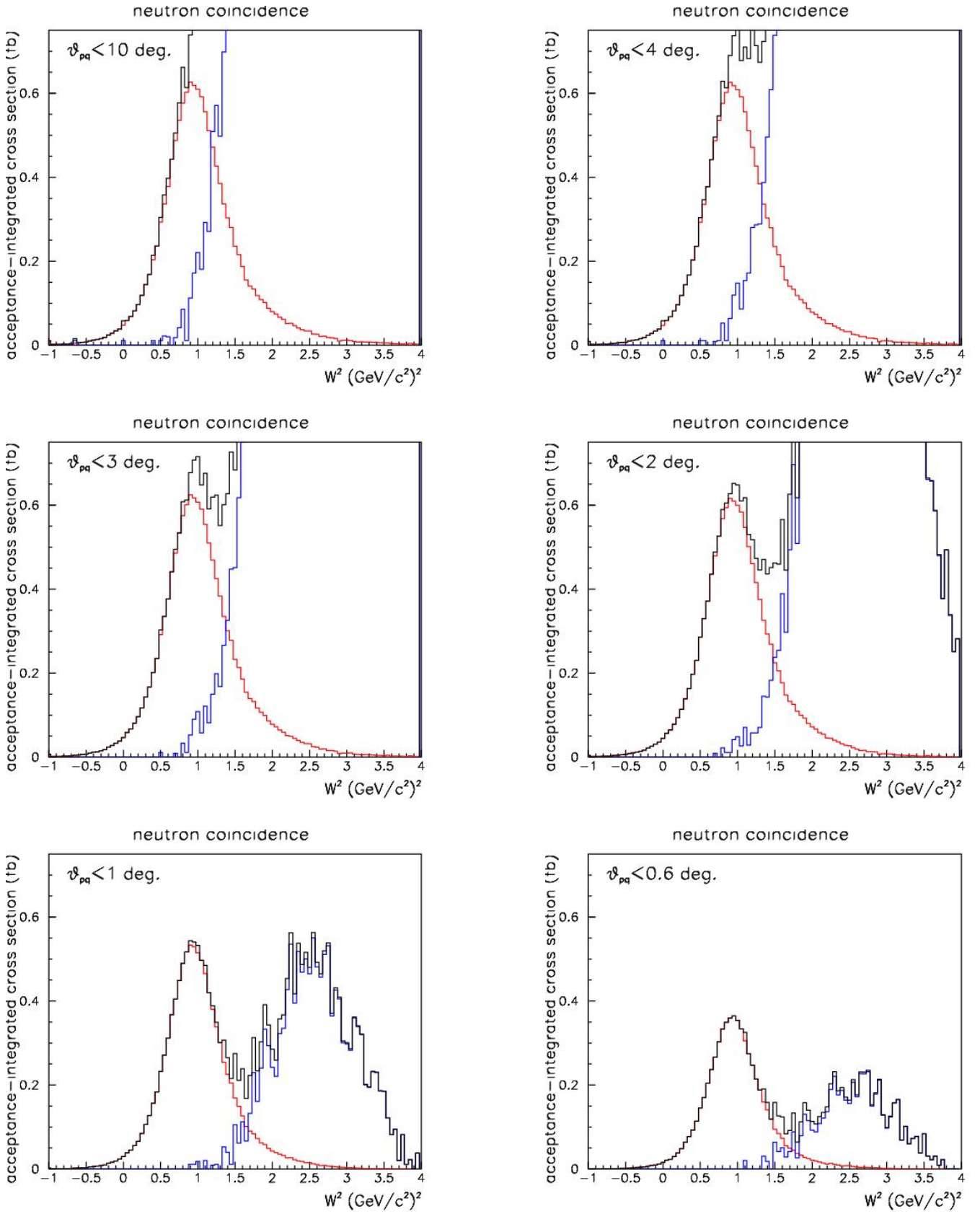
Figure 25: Quasi-elastic (red) and inelastic (blue) cross-section vs. W^2 with coincident neutron detection with different cuts on θ_{pq}. The cuts applied are (from upper left to lower right): $\theta_{pq} < 10°$, $\theta_{pq} < 4°$, $\theta_{pq} < 3°$, $\theta_{pq} < 2°$, $\theta_{pq} < 1°$, $\theta_{pq} < 0.6°$.

46

Table 7: Estimated fractional contamination of inelastic events in the quasi-elastic sample after W^2 cuts but *before any correction is applied*

Q^2 (GeV/c)^2	3.5	4.5	5.25	6.0	7.0	8.0
Proton contamination (%)	1.6	3.2	9.0	8.0	4.2	3.8
Neutron contamination (%)	2.15	7.2	6.0	18.	7.8	4.7

seen to improve as the cut is tightened. For a cut tighter than $\theta_{pq} < 2°$ the accepted quasi-elastic coincidence cross section is seen to decrease (as expected from the θ_{pq} plot shown in Fig. 24). The spectra for the $\theta_{pq} < 2°$ cut indicate that the inelastic background can be essentially eliminated by a cut of $W^2 < 1$ GeV^2 at a cost of 46% of the quasi-elastic acceptance. A cut at 1.3 GeV^2 would admit 77% of the signal and keep the inelastic contamination at only about 5%. In that case, the inelastic contamination could be accurately predicted and corrected by extrapolating the (inelastic) θ_{pq} distribution measured at $\theta_{pq} > 2°$. The statistics vs. contamination trade-offs are similar at the other Q^2 points but inelastic contamination is predicted to be larger at $Q^2 = 6$ (GeV/c)^2. The final choice of W^2 cut used in the analysis will be data-driven, based on the measured inelastic (large θ_{pq}) distribution and the inferred systematic error associated with this correction. For rate estimates, we will assume a cut at $W^2 = 1.3$ GeV The resulting estimated inelastic contamination rates (before correction) are shown in Table 7.

9 Rates

In this section we review the inputs used in the rate calculations and give the expected rates for the quasi-elastic coincidence measurements and for the calibration reactions.

Since background rates are roughly proportional to the number of target nucleons, rate estimates are based on a luminosity of $\mathcal{L} = 10^{37}/A$ cm^{-2}s^{-1}, where A is the number of nucleons in the target. This is consistent with our experience in the GEn experiment [40] using the same equipment. The observed rate of accidental events above threshold in BigHAND was ≈ 2 MHz for that measurement. The detectors will be significantly further back from the target (17 m compared to 6.5 to 12 m for GEn running) so a much smaller solid angle is subtended.

For all rate calculations the track-reconstruction efficiency in BigBite was taken to be 75% and the trigger live time was taken to be 80%. The estimated efficiencies for neutron and proton detection (shown in Fig. 5) are given in Table 8.

The cross section for quasi-elastic scattering was numerically integrated over the combined acceptance of BigBite and BigHAND, subject to the fiducial cut, as described in section 7.1. The integrals, labeled as "$\int \frac{d\sigma}{d\Omega} d\Omega$", are given in Table 8. The line labeled "W^2 cut" gives the fraction of quasi-elastic events surviving the cuts described in the previous section to reject inelastic events. Defining $\mathcal{L}_0 = 10^{37}$ cm^{-2}s$^{-1} = 36$/fb/hr, the luminosity for the quasi-elastic measurements on deuterium will be $\mathcal{L}_0/2 = 18$/fb/hr. The resulting predicted rates of electron-nucleon coincidences are given in the first two lines of Table 9.

For proton efficiency measurements using elastic scattering on Hydrogen, the full combined solid angle of BigBite and BigHAND can be used. This is given as "Full $\Delta\Omega$" in Table 8. The (scaled

Table 8: Values used in calculating count rates.

Q^2 (GeV/c)^2	3.5	4.5	5.25	6.0	7.0	8.0
E (GeV)	4.	4.	5.	5.	6.	6.
θ_e	37.5°	49.5°	40.4°	48.1°	42.0°	52.°
p efficiency (%)	78.4	86.0	90.1	93.8	96.5	97.6
n efficiency (%)	73.0	80.9	84.7	86.6	89.8	90.6
Quasi-elastic						
p-coinc. $\int \frac{d\sigma}{d\Omega} d\Omega$ (fb)	172	293	228	124	85.5	27
n-coinc. $\int \frac{d\sigma}{d\Omega} d\Omega$ (fb)	74	131	102	60	40.6	12.4
W^2 cut (%)	98	92	89	84	80	77
Proton elastic (calibration)						
Full $\Delta\Omega$ (mSr)	39.5	53.6	—	53.4	—	53.2
$\frac{d\sigma}{d\Omega}_{p(e,e')}$ (pb/sr)	71.3	10.9	—	3.00	—	0.57
$p(\gamma, \pi^+)n$ (calibration)						
$\int \Gamma dk$	0.0030	0.0039	—	0.0028	—	0.0025
$\theta^*_{\gamma\pi}$	93°	110°	—	114°	—	123°
$\frac{d\sigma}{d\Omega}_{p(\gamma,\pi^+n)}$ (pb/sr)	2380	1730	—	626	—	313

dipole approximation) cross section is also given. For this calibration on an LH2 target, the full luminosity $\mathcal{L}_0$ can be used. The resulting rates are given in the third line of Table 9. Dashes indicate the kinematic points for which proton efficiency will be estimated by interpolation rather than calibration runs.

For the neutron efficiency measurements using the $p(\gamma, \pi^+ n)$ reaction the full combined solid angle, "Full $\Delta\Omega$" can again be used. Because the 6% radiator will approximately quadruple the reaction rates in the target, the luminosity must be reduced to $\mathcal{L}_0/4$. Table 8 gives the number of useful end-point photons per incident electron ($\int \Gamma dk$), from Table 6. Dashes indicate the kinematic points for which neutron efficiency will be estimated by interpolation rather than calibration runs. Table 8 also lists the center of mass angle, $\theta^*_{\gamma\pi}$, for the (γ, π^+) reaction and the estimated cross section for the reaction. The latter is calculated using the scaling predicted by the constituent counting rule:

$$s^7 \frac{d\sigma}{dt} = \text{constant}$$

where s and t are the Mandelstam variables (invariant mass squared and four-momentum transfer squared). The constant value was conservatively taken to be 0.5×10^7 GeV^{14} nb/GeV^2 at $\theta^*_{\gamma\pi} = 90°$ based on measurements [51] made in the range of s of interest. The cross section for the actual $\theta^*_{\gamma\pi}$ was then found based upon an empirical fit [52] to the angular distribution:

$$s^7 \frac{d\sigma}{dt} = (1 - \cos\theta^*_{\gamma\pi})^{-5}(1 + \cos\theta^*_{\gamma\pi})^{-4}$$

Finally $\frac{dt}{d\cos\theta}$ was numerically evaluated to convert from $\frac{d\sigma}{dt}$ to $\frac{d\sigma}{d\Omega}$. The resulting estimated count rates are given in the last line of Table 9.

Table 9: Predicted coincidence rates (counts per hour)

Q^2 (GeV/c)^2	3.5	4.5	5.25	6.0	7.0	8.0
$d(e, e'p)$	1400	2500	1700	1050	710	220
$d(e, e'n)$	570	1050	830	470	315	93
$p(e, e'p)$	47000	11000	—	3200	—	640
$p(\gamma, \pi^+ n)$	1100	1580	—	440	—	200

Table 10: Estimated contributions (in percent) to systematic errors.

Q^2 (GeV/c)^2	3.5	4.5	5.25	6.0	7.0	8.0
Nuclear correction, G_E^n, proton cross-section	-	-	-	-	-	-
Accidentals	-	-	-	-	-	-
Target windows	.2	.2	.2	.2	.2	.2
Acceptance losses	.5	.5	.5	.5	.5	.25
Inelastic contamination	.1	.4	.3	1.	.36	.1
Nucleon mis-identification	.6	.6	.6	.6	.6	.6
BigHAND calibration	0	.13	2.8	.16	1.5	.32
Total (quadrature sum)	.81	.91	2.9	1.3	1.7	.76

10   Systematic Errors

In this section we will estimate (or set upper limits on) contributions to the systematic error on the ratio R determined by this experiment. This sets the scale for the statistical accuracy for which we should aim since it would be pointless to achieve statistical errors which are much smaller than the systematic errors.

The use of the ratio method eliminates many potential sources of systematic error. Because $d(e, e'p)$ and $d(e, e'n)$ are measured simultaneously, their ratio is insensitive to target thickness, target density, beam current, beam structure, live time, trigger efficiency, electron track reconstruction efficiency, etc. So the fractional error achieved on the ratio can be much smaller that which could be achieved on the measurement of either cross section in itself.

Table 10 lists the estimated contributions to systematic errors, which are discussed in detail below.

The corrections needed to convert from the measured value R'' (Equation 1) to the quantity of interest , R (Equation 2) are only of the order of 1%, so systematic errors on them will be neglected. The errors on the proton elastic cross section (needed to extract G_M^n from R) will not be counted towards the systematic errors of this measurement since subsequent improvements in proton cross section measurements can be combined with the R values from this experiment to improve the extraction of G_M^n .

Accidental coincidences of background events in BigHAND are not expected to cause significant

systematic errors. Previous experience in the GEn experiment [40] showed a background rate of $\approx$2 MHz across the entire detector at a three times higher luminosity. (Although the luminosity viewed by BigBite was similar to what we propose, the luminosity viewed by BigHAND was roughly three times higher than for the present proposal.) BigHAND will be significantly further from the target for this measurement so lower rates may be expected. Even with a 1 MHz rate, the probability of an accidental coincidence within a 5 ns timing gate will be only 0.5% across the entire detector. The area searched for coincident protons or neutrons is limited by the $\theta_{pq} < 2°$ cut to about 1.1 m^2 of the 8.4 m^2 face. So the rate of accidental coincidences is expected to be less than 0.07% for each nucleon species. Furthermore, this accidental contamination can be accurately estimated and subtracted by measuring the accidental coincidence rate in other parts of BigHAND, where true coincidences are not expected.

The target windows contain about 3.4% as many nucleons as the LD2 target. We use this as an upper limit on the background contribution since many of the events from aluminum will be rejected by the $\theta_{pq} < 2°$ cut. This contribution will be subtracted off by running on a dummy target with thick aluminum windows. It should be possible to apply this correction with at least 5% accuracy (allowing for uncertainty in window thickness). So the systematic error on the correction should be under 0.17%.

10.1 Acceptance Losses

As discussed above, loss of nucleons from the acceptance of BigHAND can cause a systematic error, to the extent that the losses differ for neutrons and protons. At the higher Q^2 points, the distribution of nucleons (shown in Fig. 11) are centered in BigHAND, with only modest acceptance losses. At the lower Q^2 points a fiducial cut will be applied to select events which are similarly centered in BigHAND (as discussed in section 5) so the acceptance losses are kept small. As shown in Table 4, the acceptance corrections are less than 5% in all cases, and only 2.5% at the highest Q^2 point. These losses result from the high momentum tail of the deuteron wave-function, which is identical for the neutron and proton. The cause of a difference in the corrections for the two nucleon species would be a difference in placement of the proton and neutron 'images' relative to the edges of BigHAND. It is probably conservative to allow for a possible 10% uncorrected difference in these 5% corrections, constributing 0.5% systematic error at the three lowest Q^2 points and 0.25% at $Q^2 = 8$ (GeV/c)^2.

This systematic error can be investigated (and perhaps even reduced) by examining the stability of the extracted ratio, R, as the fiducial cut is tightened or loosened from its normal value. Additionally, choosing a "window-frame" fiducial which preferentially selects events scattered near the edge of the BigHAND acceptance would allow investigation of the actual loss of protons and neutrons, which can be compared to Monte-Carlo estimates. Perhaps more importantly, such a study can be used to determine how closely the fractional losses of neutrons and protons are matched.

10.2 Inelastic Contamination

With the W^2 cuts described at the end of section 8 the predicted residual contamination of inelastic events in the quasi-elastic sample *before any corrections are made* are given in Table 7. These may be overestimated since the kinematics used for the inelastic simulation tend to exaggerate the effects of Fermi broadening. In the ratio R the contamination tends to cancel. More importantly, it should be

possible to accurately estimate and subtract the inelastic contamination. The θ_{pq} distribution (such as that shown in Fig. 24) beyond 2° gives a clear measure of the amount of inelastic contamination. Furthermore, the measured distribution can be extrapolated to small angle to accurately estimate the residual contamination. If the estimated contamination were more than ≈ 10 percent, the W^2 cuts would be tightened to reduce the contamination. In that respect this source of systematic errors does not set a limit to the useful statistical error as this systematic error can always be reduced at the cost of statistics. It should certainly be possible to estimate the inelastic contamination at the 10% level. Assuming the numbers in Table 7 are reduced by such a factor, the contributions to systematic errors will not exceed 1%.

10.3 Nucleon mis-identification

Because of the long tail of the momentum distribution of the deuteron wave-function, some nucleons will be displaced far from the position predicted based on their $\vec{q}$ vector and charge. This will result in mis-identification if a neutron is displaced sufficiently far upwards or a proton sufficiently far downwards. In the model used for the deuteron wave-function, about 5% of the nucleons have a component of momentum exceeding 100 MeV/c in any chosen direction. With a 200 MeV/c 'kick' being given to protons by the dipole, this would result in 5% mis-identification rates. The cut on W^2 preferentially rejects events with large Fermi momentum, however and so the mis-identification rate is reduced to 3% or less for the cuts considered here. The misidentification of one species as the other and *vice versa* do not cancel because the proton rate is higher and protons have a higher efficiency of being detected. If the mis-identification went uncorrected, the number of detected 'neutrons' would be increased by proton contamination while the number of detected 'protons' would be decreased by a loss of protons which would not be offset by misidentified neutrons. Thus the effect would be an overestimate of R. The fractional overestimate of R depends on the actual ratio of proton/neutron cross sections and efficiencies. Taking the ratio of cross sections to be $\frac{d\sigma}{d\Omega}\big|_p / \frac{d\sigma}{d\Omega}\big|_n \approx 2.4$ and the detection efficiencies to be $\epsilon_p = 80\%$ and $\epsilon_n = 75\%$, this 3% kinematic spread of nucleons would cause the neutron rate to be overestimated by 4.7% and the protons to be underestimated by 1.8% and so R would be overestimated by 6.6%.

The contamination will not go uncorrected, however, and at least two techniques will be used to measure this kinematic tail. The neutron tail below the predicted point on the face of BigHAND can be measured without contamination from protons. Similarly the proton tail above the predicted point on BigHAND will be free of neutrons. Symmetry can then be used to predict the contamination of neutrons in the proton peak and, with minor kinematic corrections because of the deflection magnet, the proton contamination of the neutron peak. Since these tails originate from the same Fermi motion, the neutron and proton tails should be almost identical apart from minor distortion due to the deflection magnet. Another technique for determining the tails in the 'contamination region' will be to use the vetos to preferentially select neutrons or protons. In particular a clean sample of neutrons can be selected (with only a few percent proton contamination, which can be subtracted off) to separately determine the kinematic spread. It should be possible to measure at the 10% level, the 'leakage' of neutrons/protons into the regions in which the other species is expected. A 10% error in the measurement of such a 3% tail would cause a systematic error of $\approx 0.6\%$ in the extracted value of R.

10.4 Nucleon Detection Calibration

There are several potential issues involved in determining the systematic errors associated with the calibration of the BigHAND efficiencies for detection of neutrons and protons. A useful attribute of the $p(\gamma, \pi^+)n$ reaction is that the neutrons used for calibration have essentially the same energy as those in the middle of the quasielastic peak. This is a significant advantage relative to our previous CLAS experiment [37,39] at lower Q^2 in which $p(e, e'\pi^+)n$ was used for calibration. There, the three-body final state gave lower neutron energies than those of interest so it was necessary to parameterize the efficiency as a function of energy to estimate the efficiency at the energy of interest. Thus, the largest source of systematic errors in the earlier experiment is avoided here.

In principle the statistical error on the calibration of the detection efficiencies represents a systematic error on the measurements of the quasi-elastic reaction of interest. In fact it is not prohibitive to obtain sufficient statistics on the calibration reaction so that the error on the efficiencies are comparable to the statistical error on the quasi-elastic measurements. We treat this as a statistical error in subsequent discussions, and so don't include it in Table 10.

As shown in Table 5, up to 11.4% of the quasi-elastic nucleons (in the $Q^2 = 8$ (GeV/c)^2 case) will fall outside the region which can be calibrated at elastic kinematics at the same beam energy and BigHAND position. The "uncalibrated" regions of the detector could reasonably be assigned the average efficiency obtained from the calibration, since they share the same shower-generation geometry and are, in fact, mostly just different positions on the same physical detector bars. A further refinement can be made, as has been described in section 6.3, by extrapolating calibrations made at lower energies to take into account the slightly different interaction probability. Since the efficiency is high, and unlikely to change rapidly, it is unreasonable to expect the efficiency in the "uncalibrated" region to differ by more than 2% from the efficiency predicted by these methods, as the actual change in efficiency from one calibration point to the next (shown in Table 8 and Fig. 5 does not exceed 8% from one calibration point to the next. (Copious calibration data will be taken at the low Q^2 point, so any anomalous regions, such as dead PMT's will be identified and either repaired or corrected for.) We assign an upper-limit systematic error of 2% of the fraction of the events which fall outside the calibrated region. Since this error appears in both the numerator and denominator of R, it is multiplied by $\sqrt{2}$ to give an error of 2.8% of the fraction of nucleons outside the calibrated region (found from the last column of Table 5).

For the $Q^2 = 5.25$ and 7 (GeV/c)^2 points, the BigHAND efficiency will be estimated by interpolation of calibration points at higher and lower Q^2. (As described above, the interpolation will be guided by the expected efficiency variation so an 'effective thickness' will be interpolated.) Table 8 shows that the total change in efficiency between the points at $Q^2 = 4.5$ and 6.0(GeV/c)^2 is only 5.7% for neutrons and 7.8% for protons. Taking one quarter of this range as a generous estimate of the error bar on the interpolation of the efficiency to $Q^2 = 5.25$ (GeV/c)^2 for each species gives a systematic error on the efficiency-corrected ratio of 2.8%. Similarly interpolation to $Q^2 = 7$ (GeV/c)^2 would be assigned errors of one quarter of 4% and of 3.8% for neutrons and protons respectively, to give an error of 1.5% on the efficiency-corrected ratio.

The final line of Table 10 shows the estimated total systematic error on R, found by adding the individual contributions in quadrature. In summary the systematic errors are expected to contribute about a 1% to 3% error on R.

11 Installation

The BigBite detector upgrade is already planned and will be carried out independently of this experiment. A significant upgrade of the BigHAND electronics is planned, to reduce the dead time of the veto detectors. That can be carried out independently of Hall operations.

Two major pieces of equipment will need to be installed in the Hall for this experiment.

The BigHAND nucleon detector has been used in the past [40] and so there is operational experience on rigging it in and out of the Hall. In preparation for the GEn experiment, it was rigged into the Hall in six weeks, with no previous operational experience and with the BigBite spectrometer being rigged in parallel.

The 48D48 (BigBen) 'spectrometer' magnet (here being used as a particle-identification magnet) is available from BNL but will required major modifications in advance of installation to allow it to be placed close to the beam line without mechanical or magnetic interference with the beam on its way to the beam dump. We expect to play a leading role in the magnetic and mechanical design for modifications to the magnet and for beam line shielding and/or correctors. We will also participate in the design of mechanical systems to allow the magnet to be re-positioned for different scattering angles. It is important to note that these modifications are needed independently for an already-approved [53] 12 GeV experiment. The impact of the proposed experiment would be to move up the timetable for these modifications and mechanical support systems.

Based on past experience, including the installation of the GEn experiment, we estimate that six to eight weeks will be required to install the equipment needed for this experiment. Ideally, of course, this will be carried out during an accelerator down-time.

12 Beam Time Request

Based on the systematic error estimates in Table 10 we could set a goal of 2% statistical errors on the deterimination of R at the 4 Q^2 points at which BigHAND calibrations are done and 3% at $Q^2 = 5.25$ and 7 $(\text{GeV/c})^2$. This is the quadrature sum of the fractional errors on the number of proton coincidences, the number of neutron coincidences, the proton efficiency and the neutron efficiency. So each of these terms must be measured with roughly half that statistical error. (In principle beam time can be optimized by measuring the efficiencies with smaller fractional error allowing larger error on the coincidence measurements. There is limited margin for optimization however, and systematic errors on the efficiencies would then play a disproportionate role.) The beam time required for the highest Q^2 point would then be large because of the small neutron-coincident count rate. So we relax our goal to a 3% statistical error in R at $Q^2 = 8$ $(\text{GeV/c})^2$ (corresponding to 1.5% contribution on each of the components combined in quadrature).

The scale of beam time required for deuteron running is then set by the requirement of N= 10^4 statistics in the neutron coincident measurements at $Q^2 = 3.5$, 4.5, and 6 $(\text{GeV/c})^2$ (and N=4500 for the other three Q^2 points). Because binomial statistics apply for the efficiency measurements, the number of required events is considerably smaller. If N_{in} particles are incident on the detector, each with probability p of being observed, then the variance on the number of observed particles N_{obs} is

$$\sigma^2 = N_{in} \, p(1-p) \approx N_{obs} \, (1-p)$$

Table 11: Beam Time Request (beam hours)

Q^2 (GeV/c)^2	3.5	4.5	5.25	6.0	7.0	8.0	
E (GeV)	4.	4.	5.	5.	6.	6.	
θ_e	37.5°	49.5°	40.4°	48.1°	42.0°	52.°	
d(e, e')							
Normal $\mathcal{L}$	36	24	24	48	36	80	
Dummy target	3	2	2	4	3	8	
Half $\mathcal{L}$	12	6					
Dummy half $\mathcal{L}$	2	1					
H(e, e')							
Normal $\mathcal{L}$	24	6		6		6	
Half $\mathcal{L}$	3	3		6		6	
Quarter $\mathcal{L}$	3	6					
BigBen off	6	6		6		6	
Dummy target	4	1		1		1	
H(γ, π^+)							
Radiator	24	24		12		20	
Dummy target	3	3		2		3	
No radiator	6	6		3		5	
Total	126	88	26	88	39	136	$\Rightarrow$ 502
Commissioning							72
2 Energy changes							16
13 angle changes							52
8 polarity changes							32
Beam request							674
							$\approx$28 days

So the fractional error in the efficiency $\eta = N_{obs}/N_{in}$ is

$$\frac{\sigma_\eta}{\eta} = \frac{\sigma}{N_{obs}} = \frac{\sqrt{1-p}}{\sqrt{N_{obs}}}$$

The required statistics for a given fractional error is therefore reduced by a factor of $(1-p)$ compared to counting statistics. With conservatively estimated neutron and proton efficiencies of at least $p_n = 0.70$ and $p_p = 0.75$ this reduces the required number of calibration coincidences by factors of 0.3 and 0.25, respectively, from the numbers quoted above for the quasi-elastic neutron coincidence measurements.

Using these considerations along with the rates given in Table 9 to determine the minimum data taking time in each configuration, estimated beam times are tabulated in Table 11. In some cases the requested time greatly exceeds the minimum to allow us to take advantage of data which is readily available. The proton calibration rate is so high at the lowest Q^2 point point, for example,

that adequate statistics could be acquired in about 10 minutes. This high rate provides an excellent opportunity to study efficiency variation across the face of BigHAND, so far more data taking time is scheduled. Just 24 hours of running will give a million events, allowing the BigHAND face to be finely subdivided and precisely calibrated in many separate regions. For several calibration points or high-rate quasi-elastic points we also allow time for running at reduced luminosity to ensure that accidental rates are well understood. Elastic scattering measurements with the 48D48 deflector dipole turned off will be useful for checking the alignment of the $\vec{q}$ inferred from BigBite measurements with the actual hit positions in BigHAND. For the neutron calibration, time is included for running without a radiator to measure the virtual photon contribution. Time is also allowed for running on dummy targets for subtraction of target window contributions. Eight hours are allowed for each beam energy change. In addition to the time required to position the spectrometers for each measurement, each elastic calibration requires two spectrometer-moves and two reversals of the BigBite polarity. Four hours are allowed for each operation. Finally, 72 beam hours are requested for commissioning of the system including the new 48D48 deflector magnet. In total, 28 days are requested.

Figure 26 shows the size of the errors on the extracted values of G_M^n which would be obtained with the desired statistics and the systematic errors given in Table 10 (added in quadrature). The value is arbitrarily plotted at unity. The fractional error on R has been scaled down by a factor of two to give the fractional error on G_M^n . The final fractional error in G_M^n is under 2.5% (i.e. less than 5% error on R) for all Q^2 points. (Note that the highest Q^2 SLAC point, shown in Fig. 1 is off-scale in this more-enlarged plot.)

13   Relation to Other Experiments

This experiment uses much of the same detector equipment as the GEn experiment (E02-013) [40] and many of the collaborators most involved in that experiment are also involved here. Technical expertise in tracking in BigBite and in calibration of BigHAND will be available for this analysis. The large dipole magnet, which is proposed for deflection of protons, is a part of an approved 12 GeV experiment which will measure Electric Form Factor of the proton at very large Q^2 [53].

High precision measurements of the neutron magnetic form factor were made at lower Q^2 in the CLAS e5 measurement (E94-017). Many of the principle people involved in the analysis [39] of that dataset are involved in the present proposal. This measurement will complement the CLAS measurement by extending the precision measurements to almost twice as high a Q^2. We will draw on much expertise and experience in controlling systematic errors in such a ratio measurement.

A 12 GeV experiment (E12-07-104) has recently been approved to extend the high-precision measurements of G_M^n out to beyond $Q^2 = 13$ (GeV/c)^2 using the CLAS12 detector. Three of the spokespersons of that experiment are also involved in the present proposal. The results from the two experiments will be complementary in that the CLAS12 data will have larger systematic errors (3% error on G_M^n) but will cover a larger range of Q^2 with contiguous coverage which can be subdivided into many data points. The proposed experiment would measure only at six Q^2 values (and not go beyond $Q^2 = 8$ (GeV/c)^2) but aims to have significantly smaller systematic and statistical errors. CLAS12 is a large-acceptance device which, by its nature, collects data simultaneously at many scattering angles but with low luminosity. The proposed experiment collects data only at predetermined angles but can run at far higher luminosity (the planned luminosity for this proposal
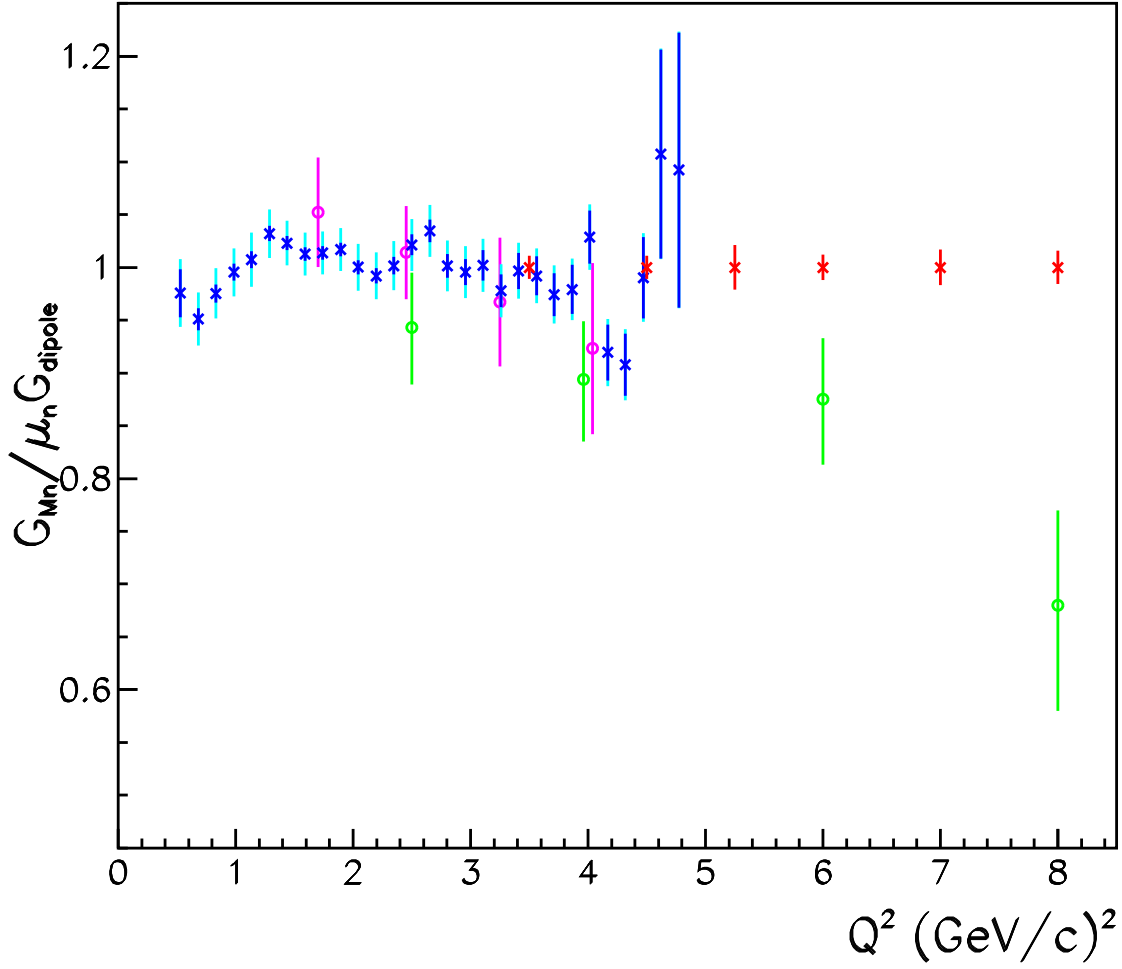
Figure 26: Existing data on G_M^n in the Q^2 range of the proposed measurement are plotted as ratio to scaled dipole approximation. (See caption of figure 1.) Red points (arbitrarily plotted at unity) show projected size of error bars for this experiment.

is 100 times the design luminosity for CLAS12). Systematic errors are more easily controlled for single-position detectors than for large acceptance detectors. The use of the same detector for both nucleon species also helps control the systematic errors in the proposed measurement. In the present proposal, the large baseline between the target and the hadron detector (17 m) also provides a major advantage in selection of quasi-elastic events due to superior angular and momentum resolution.

Our experience on the CLAS e5 experiment showed it to be very valuable to have overlapping measurements. There, two beam energies and two neutron detection systems allowed up to four redundant measurements in some regions. This was beneficial as a way to protect against unsuspected systematic problems in each of the measurements. Ultimately each of the experiments will benefit from the partial overlap of the kinematic coverage. Of course, since the present experiment uses the existing 6 GeV JLab beam, it would run earlier and produce results much earlier than the CLAS12 experiment. The CLAS12 data will serve as a useful check (and hopefully confirmation) of the results of the present proposal. Inspection of the present data (Fig. 26) suggests that the proposed measurement must either see an abrupt change in the behavior of the form factor in this kinematic range or be in conflict with either the CLAS [39] or SLAC [26] data sets. In any of those cases, the CLAS12 data would then be an important confirmation.

While no future experiment has yet been designed, it is likely that we will consider the possibility of extending this technique to measure higher Q^2 points after the the 12 GeV upgrade. It is important to note, however, that the higher beam energy would offer no advantage for the measurements proposed here. Especially for neutron efficiency calibration by the bremsstrahlung endpoint method, it is important that the beam energy not be too high, or it becomes impossible to resolve the required two-body final state. In fact for several of our measurements, it is an advantage to use a lower beam energy than the maximum presently available.

References

[1] M.N. Rosenbluth, Phys. Rev. **79** 615 (1950).

[2] M.K. Jones *et al.*, Phys. Rev. Lett.**84** 1398 (2000).

[3] O. Gayou *et al.*, Phys. Rev. Lett.**88** 092301 (2002).

[4] A.V. Afanansev *et al.*, Phys. Rev. D **72** 013008 (2005).

[5] G. Miller, Phys. Rev. Lett. **99** 112001 (2007).

[6] D. Kaplan and A. V. Manohar, Nucl. Phys. B **310**, 527 (1988)

[7] R. D. McKeown, Phys. Lett. B **219**, 140 (1989)

[8] D.H. Beck, Phys. Rev. D **39**, 3248 (1989)

[9] D. Müller, D. Robaschik, B. Geyer, F.M. Dittes, J. Horejsi, Fortsch. Phys. 42 (1994) 101.

[10] X. Ji, Phys. Rev. Lett. **78**, 610 (1997); Phys. Rev. D **55**, 7114 (1997).

[11] A.V. Radyushkin, Phys. Lett. B **380**, 417 (1996); Phys. Lett. B **385**, 333 (1996); Phys. Rev. D **56**, 5524 (1997).

[12] T. Eden *et al.*, Phys. Rev. C **50**, R1749 (1994).

[13] M. Ostrick *et al.*, Phys. Rev. Lett. **83**, 276 (1999).

[14] C. Herberg *et al.*, Eur. Phys. Jour. A **5**, 131 (1999).

[15] Jefferson Lab experiment E93-038, spokespersons: R. Madey, S. Kowalski.

[16] I. Passchier *et al.*, Phys. Rev. Lett. **82**, 4988 (1999).

[17] H. Zhu *et al.*, Phys. Rev. Lett. **87**, 081801, 2001.

[18] M. Meyerhoff *et al.*, Phys. Lett. B **327**, 201 (1994).

[19] H. Gao *et al.*, Phys. Rev. C **50**, R546 (1994); H. Gao, Nucl. Phys. A **631**, 170c (1998).

[20] W. Xu *et al.*, Phys. Rev. Lett. **85**, 2900 (2000).

[21] W. Xu *et al.*, Phys. Rev. C. **67**, R012201 (2003).

[22] E.B. Hughes *et al.*, Phys. Rev. **139**, B458 (1965); *ibid.* **146**, 973 (1966).

[23] B. Grossetête, S. Jullian, and P. Lehmann, Phys. Rev. **141**, 1435 (1966).

[24] A.S. Esaulov *et al.*, Sov. J. Nucl. Phys. **45**, 258 (1987).

[25] R.G. Arnold *et al.*, Phys. Rev. Lett. **61**, 806 (1988).

[26] S. Rock *et. al.*, Phys. Rev. D **46** 24 (1992).

[27] A. Lung *et al.*, Phys. Rev. Lett. **70**, 718 (1993).

[28] R.J. Budnitz *et al.*, Phys. Rev. **173**, 1357 (1968).

[29] K.M. Hanson *et al.*, Phys. Rev. D **8**, 753 (1973).

[30] P. Stein *et al.*, Phys. Rev. Lett. **16**, 592 (1966).

[31] W. Bartel *et al.*, Phys. Lett. B **30**, 285 (1969); *ibid.* **39**, 407 (1972); Nucl. Phys. B **58**, 429 (1973).

[32] P. Markowitz *et al.*, Phys. Rev. C **48**, R5 (1993).

[33] H. Anklin *et al.*, Phys. Lett. B **336**, 313 (1994).

[34] E.E.W. Bruins *et al.*, Phys. Rev. Lett. **75**, 21 (1995).

[35] H. Anklin *et al.*, Phys. Lett. **B428**, 248 (1998).

[36] G. Kubon *et al.*, Phys. Lett. **B524** 26 (2002).

[37] JLab Experiment E94-071
"The Neutron Magnetic Form Factor from Precision Measurements of the Ratio of Quasielastic Electron-Neutron to Electron-Proton Scattering in Deuterium", W. Brooks and M. Vineyard spokespersons

[38] L. Durand, Phys. Rev. **115** 1020 (1959).

[39] J, Lachniet thesis, Carnegie Mellon University, unpublished, June, 2005
http://www-meg.phys.cmu.edu/ bquinn/jeff_thesis.pdf

[40] JLab experiment E02-013, G.Cates, N.Liyanage and B.Wojtsekhowski (spokespersons)

[41] S.Riordan, private communication

[42] See proposal of JLab Experiment E12-06-122 "Measurement of neutron asymmetry A_1^n in the valence quark region using BigBite spectrometer." G.Cates, N.Liyanage , Z.Meziani, G.Rosner, X.Zheng and B.Wojtsekhowski (spokespersons)

[43] Rob Feuerbach, private communication

[44] S.Abrahamyan, GEANT-4 simulation with saturation effect in light output.

[45] J.L. Matthews and R.O. Owens, Nucl. Instr. and Meth. **111**, 157 (1973)

[46] E.L. Lomon and H. Feshbach, Annals of Phys. **48** 94 (1968).

[47] E12-07-108 proposal

[48] Data from PDG, http://pdg.lbl.gov/xsect/contents.html and references therein.

[49] M.Ripani and E.M.Golovach based on P.Corvisiero, *et al.*, Nucl. Instr. and Meth. A, **3464** 33 (1994).

[50] L.M. Stuart, *et. al.*, Phys. Rev. D **58** 032003 (1998).

[51] L.Y. Zhu, *et. al.*, Phys. Rev. C **71** 044603 (2005)

[52] R.L. Anderson, *et al*, Phys. Rev. D **14** 679 (1976).

[53] JLab E12-07-109, Ch. Perdrisat *et al*, Large Acceptance Proton Form Factor Ratio Measurements at 12 and 15 $(\text{GeV}/c)^2$ Using Recoil Polarization Method.